

Computer Methods in Applied Mechanics and Engineering 00 (2020) 1-23

Computer methods in applied mechanics and engineering

A third order, implicit, finite volume, adaptive Runge-Kutta WENO scheme for advection-diffusion equations

Todd Arbogast^a, Chieh-Sen Huang^b, Xikai Zhao^c, Danielle N. King^d

^aDepartment of Mathematics, and Institute for Computational Engineering & Sciences, The University of Texas at Austin, Austin, TX 78712 (arbogast@ices.utexas.edu)

Abstract

A finite volume approximation of the scalar hyperbolic conservation law or advection-diffusion equation is given. In the context of the method of lines, the space discretization uses weighted essentially non oscillatory (WENO) reconstructions with adaptive order (WENO-AO), and the time evolution uses implicit Runge-Kutta methods. Therefore the timestep may be larger than the CFL timestep. To reduce oscillation in the solution, ideas related to spatially partitioned Runge-Kutta methods are used. An adaptive Runge-Kutta method is developed that blends the L-stable, third order, implicit Radau IIA method with the composite backward Euler method using a weighting procedure inspired from spatial WENO methods. The weighting procedure requires a smoothness indicator, and several possibilities are considered, although one is perhaps seen to be preferred. The overall scheme is proven to maintain third order accuracy when the solution is smooth. When the solution has a discontinuity, the scheme is shown computationally to be third order accurate away from shocks, and to achieve the overall accuracy of the backward Euler method. Numerical examples show that the adaptive Runge-Kutta method reduces oscillations in the solution. Moreover, the resulting scheme is shown to be unconditionally L-stable for smooth solutions to the linear problem.

Keywords: implicit WENO, von Neumann stable, L-stable, adaptive Runge-Kutta, multirate Runge-Kutta, spatially partitioned Runge-Kutta

2010 MSC: 65M08, 65M20, 65M12, 76M12

1. Introduction

We consider finite volume approximation of the scalar hyperbolic conservation law, and more generally of the advection-diffusion equation

$$u_t + f(u)_x - Du_{xx} = u_t + F(u, u_x)_x = 0, \quad x \in \mathbb{R}, \ t > 0,$$
 (1.1)

where $D \ge 0$ and $F(u, u_x) = f(u) - Du_x$. We solve the problem using the method of lines, which divides the scheme into space and time approximations. For the space discretization, we use weighted essentially non oscillatory (WENO) reconstructions with adaptive order (WENO-AO) [1, 2, 3]. For time evolution, we restrict ourselves to implicit methods, both because the problem (1.1) is stiff when D > 0 and because we would like to use timesteps larger than the CFL timestep that explicit methods are limited to. However, a high order Runge-Kutta method can generate oscillations when the timestep is large. So we develop an adaptive Runge-Kutta scheme that blends a higher order implicit Runge-Kutta method (we use third order implicit Radau IIA) and the composite backward Euler method using a weighting procedure inspired from spatial WENO methods.

^bDepartment of Applied Mathematics, National Sun Yat-sen University, Kaohsiung 804, Taiwan, R.O.C. (huangcs@math.nsysu.edu.tw)
^cDepartment of Mathematics, University of Texas, 2515 Speedway, C1200, Austin, TX 78712-1202. Currently at Schlumberger, Geophysics
Technology Center (GTC), 3750 Briarpark Dr., Houston, TX 77042. (xikaizhao@gmail.com)

^dDepartment of Mathematics, University of Texas, 2515 Speedway, C1200, Austin, TX 78712-1202 (dking3@math.utexas.edu)

1.1. Adaptive time evolution

We are particularly interested in the time evolution of (1.1). If D=0, the problem is hyperbolic and shocks and contact discontinuities may appear in the solution. If merely D is small, the solution may exhibit steep fronts, which (for finitely discretized numerical methods) also appear as if they were discontinuities in the solution. Ideally, we would use strong stability preserving (SSP) Runge-Kutta methods [4, 5, 6]. Unfortunately, there are no unconditionally stable SSP methods of order greater than one [6, 7]. We therefore restrict ourselves to L-stable Runge-Kutta methods, which can, however, produce some oscillation.

Multirate methods (see, e.g., [8, 9, 10]) and embedded multirate methods [11, 12] were developed to allow varying timesteps, and thereby achieve better resolution, i.e., less oscillation, of the solution near shocks. These methods can often be formulated as spatially partitioned Runge-Kutta methods [13, 14], which can be viewed as a method that merges two Runge-Kutta methods with the same time levels. Most often, a single Runge-Kutta method is used at any given point in space. It is possible to blend the two Runge-Kutta methods; that is, to use a weighted combination of them. For example, this is done in the partition of unity approach [15]. The weighting function is often defined in an ad hoc way.

For finite volume schemes, one normally views the method of lines as applying to the time evolution of the mesh cell. However, in this case, spatially partitioned Runge-Kutta methods will suffer from non conservation of mass unless a *flux based partitioning* [11] is applied, in which the flux on each mesh cell interface uses its own Runge-Kutta method. However, this leads to an inconsistent approximation at the interface between Runge-Kutta methods (i.e., on *transition cells*, where different Runge-Kutta methods are applied at the two interfaces of the cell), see, e.g., [9, 14, 11].

A more subtle problem with the use of spatially partitioned Runge-Kutta methods is that their convergence properties depend on the smoothness of the true solution. In the case of hyperbolic conservation laws (or advection-diffusion equations (1.1)), the solution may not be smooth. However, it is observed numerically that the backward Euler method always seems to give a good solution (see, e.g., [16]). We therefore propose to use a weighted (i.e., blended), flux-based, spatially partitioned, implicit Runge-Kutta method that combines a higher order implicit Runge-Kutta method with composite backward Euler. We will weight the methods using a procedure inspired from spatial WENO methods. This requires defining a smoothness indicator, and we will explore several possibilities and advocate for a specific choice. We will thereby provide a systematic definition of the weighting function.

We will prove that the weighting procedure does not degrade the accuracy of the adaptive Runge-Kutta approximation when the solution is smooth. When there is a discontinuity, however, the inconsistency at the interface between Runge-Kutta methods on transition cells will prevent us from proving optimal convergence. Instead, we will show computationally that the accuracy maintains third order away from the shocks, but indeed drops to that of the backward Euler method overall (which is to be expected—see [9, 14, 11]). Overall, the adaptive method reduces oscillations in the solution, and thereby allows us to take longer timesteps. Moreover, we will show that the L-stability property of the Runge-Kutta method is retained by our overall scheme, by showing that approximations to smooth solutions of the linear problem are unconditionally stable in the sense of a von Neumann stability analysis.

1.2. The finite volume framework

We close the introduction by giving the finite volume framework for approximation of (1.1). For simplicity we have assumed that D is constant, but see [17] for handling non constant, and even degenerate, diffusion.

Partition time as $0 = t^0 < t^1 < t^2 < \cdots$, and define $\Delta t_n = t^{n+1} - t^n$, $t^{n+1/2} = (t^n + t^{n+1})/2$, and, more generally for use later, $t^{n+\theta} = t^n + \theta \Delta t_n$. Partition space by grid points $\cdots < x_{-1/2} < x_{1/2} < x_{3/2} < \cdots$. Define the mesh cell or element $I_i = [x_{i-1/2}, x_{i+1/2}]$, its length $\Delta x_i = x_{i+1/2} - x_{i-1/2}$, and its midpoint $x_i = \frac{1}{2}(x_{i+1/2} + x_{i-1/2})$. Let $h = \max_i \Delta x_i$ and assume that the grid is quasi-uniform (i.e., there is some $\rho \in (0, 1]$ such that $\rho h \le \min_i \Delta x_i$, so $\rho h \le \Delta x_i \le h$ for all i).

Let $\bar{u}_i(t)$ be the average of u(x, t) on the cell I_i , i.e.,

$$\bar{u}_i(t) = \frac{1}{\Delta x_i} \int_{I_i} u(x, t) \, dx. \tag{1.2}$$

Later, $\bar{u}_i(t)$ will be an approximation to the same integral average. For a general function $\phi(x, t)$, we denote (and later approximate)

$$\phi_{i+\alpha}(t) = \phi(x_i + \alpha \Delta x_i, t) \quad \text{and} \quad \phi_{i+\alpha}^{n+\theta} = \phi(x_i + \alpha \Delta x_i, t^{n+\theta}), \tag{1.3}$$

for any $\alpha \in [-1/2, 1/2]$ and $\theta \in [0, 1]$. Integration of (1.1) in space leads to

$$\frac{d}{dt}\bar{u}_i(t) = -\frac{1}{\Delta x_i} \left[F(u_{i+1/2}(t), u_{x,i+1/2}(t)) - F(u_{i-1/2}(t), u_{x,i-1/2}(t)) \right]. \tag{1.4}$$

We introduce the Lax-Friedrichs flux, i.e.,

$$\hat{f}(a,b) = \frac{1}{2} [f(a) + f(b) - \delta(b-a)], \tag{1.5}$$

where $\delta = \max_{u} |f'(u)|$, and define

$$\hat{F}(a,b,c) = \hat{f}(a,b) - Dc. \tag{1.6}$$

The problem (1.1) is then transformed into

$$\frac{d}{dt}\bar{u}_i(t) = -\frac{1}{\Delta x_i} [\hat{F}_{i+1/2}(t) - \hat{F}_{i-1/2}(t)],\tag{1.7}$$

where $\hat{F}_{i\pm 1/2}(t) = \hat{F}(u^-_{i\pm 1/2}(t), u^+_{i\pm 1/2}(t), u_{x,i\pm 1/2}(t))$, and where $u^-_{i\pm 1/2}$ and $u^+_{i\pm 1/2}$ are left and right point values for u at $x_{i\pm 1/2}$, which later will be approximations, i.e., $u^-_{i\pm 1/2}(t) \approx u(x^-_{i\pm 1/2}, t)$ and $u^+_{i\pm 1/2}(t) \approx u(x^+_{i\pm 1/2}, t)$; moreover, $u_{x,i\pm 1/2}(t) \approx u(x^+_{i\pm 1/2}, t)$. It remains to discuss the spatial reconstruction and time integration approximations.

In the remainder of the paper, we describe the WENO-AO reconstructions that we use in the next section. In Section 3, we describe our new adaptive Runge-Kutta method. We analyze the time discretization errors in Section 4, paying attention to whether the solution is smooth or has discontinuities. In Section 5, we show that our new scheme is unconditionally stable for smooth solutions to the linear problem, using a fixed weight for the adaptive Runge-Kutta method. We discuss alternate definitions of the smoothness indicator used to adaptively weight the Runge-Kutta methods in Section 6. We end the paper with some numerical results in 1D and 2D (using Strang splitting [18]) in Section 7, and with a summary and conclusions in the final section.

2. WENO reconstructions with adaptive order (WENO-AO)

For the reconstruction of some $x \in I_i$ at a fixed time t from cell averages, consider a stencil $S^r \ni I_i$ with r contiguous cells. We can reconstruct u as a stencil polynomial $P^r(x)$ of degree r-1 by imposing the conditions

$$\frac{1}{\Delta x_k} \int_{I_k} P^r(x) \, dx = \bar{u}_k, \quad \forall I_k \in S^r.$$

Provided that u is smooth on S^r , P^r is an rth order approximation to u. The smoothness indicator defined by Jiang and Shu [19] is used to measure the smoothness of the polynomial $P^r(x)$ on the cell I_i . It is given by

$$\sigma_{P^r} = \sum_{\ell=1}^{r-1} \int_{I_i} \Delta x_i^{2\ell-1} \Big(\frac{d^{\ell}}{dx^{\ell}} P^r(x) \Big)^2 dx.$$
 (2.1)

2.1. WENO-AO(3,2) for reconstruction of left and right point values

For a third order WENO scheme, we consider the stencils depicted in Figure 2.1, from which two linear polynomials $P_{\rm L}^2$ and $P_{\rm R}^2$, as well as a quadratic polynomial $P_{\rm C}^3$ are reconstructed over $S_{\rm L}^2 = \{I_{i-1}, I_i\}$, $S_{\rm R}^2 = \{I_i, I_{i+1}\}$, and $S_{\rm C}^3 = \{I_{i-1}, I_i, I_{i+1}\}$, respectively. We use these stencils to reconstruct $u_{i-1/2}^+$ and $u_{i+1/2}^-$.

Levy et al. in [20] introduced a compact CWENO3 reconstruction, where they combined the quadratic polynomial with the linear polynomials. Balsara et al. generalized the idea of combining low order polynomials with high order polynomials to define WENO reconstructions with adaptive order [1, 3, 2]. Take any *linear weights* α_C^3 , α_L^2 , and α_R^2 as arbitrary positive numbers summing up to one. (We take $\alpha_C^3 = 1/2$ and $\alpha_L^2 = \alpha_R^2 = 1/4$.) Then the reconstruction of u at $x \in I_i$ is a convex combination of the three polynomials, defined as

$$u(x) \approx R_i^{AO}(x) = \frac{\tilde{\alpha}_C^2}{\alpha_C^3} [P_C^3(x) - \alpha_L^2 P_L^2(x) - \alpha_R^2 P_R^2(x)] + \tilde{\alpha}_L^2 P_L^2(x) + \tilde{\alpha}_R^2 P_R^2(x).$$
 (2.2)

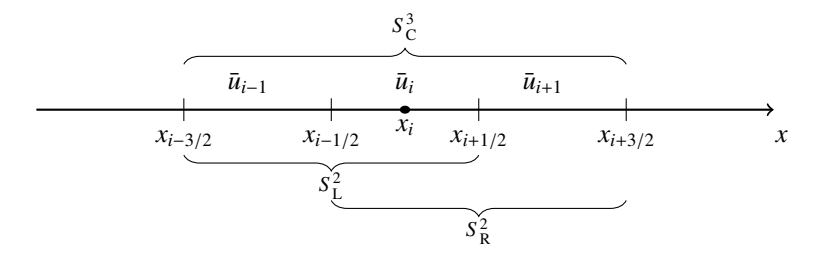


Figure 2.1: WENO-AO(3,2) stencils.

The nonlinear weights $\tilde{\alpha}_{\rm C}^3$, $\tilde{\alpha}_{\rm L}^2$, and $\tilde{\alpha}_{\rm R}^2$ are computed by

$$\hat{\alpha}_{j}^{s} = \frac{\alpha_{j}^{s}}{(\epsilon_{h} + \sigma_{P_{s}^{s}})^{\eta}}, \quad \tilde{\alpha}_{j}^{s} = \frac{\hat{\alpha}_{j}^{s}}{\hat{\alpha}_{C}^{3} + \hat{\alpha}_{L}^{2} + \hat{\alpha}_{R}^{2}}, \quad (j, s) \in \{(L, 2), (R, 2), (C, 3)\},$$
(2.3)

where the constants are usually chosen as $\eta=2$ and $\epsilon_h=10^{-6}$. However, based on [3, 2], we take $\epsilon_h=\epsilon_0h^2$ for some $\epsilon_0>0$. As in [20], one could use $\sigma_{P_{\rm cent}^3}$ in place of $\sigma_{P_{\rm C}^3}$ to define $\hat{\alpha}_{\rm C}^3$, where $P_{\rm cent}^3(x)=[P_{\rm C}^3(x)-\alpha_{\rm L}^2P_{\rm L}^2(x)-\alpha_{\rm R}^2P_{\rm R}^2(x)]/\alpha_{\rm C}^3$.

2.2. WENO-AO(4,3) for reconstruction of the derivative at a point

We need a reconstruction of u_x when $D \neq 0$. We use the same type of WENO-AO reconstruction to approximate u_x . Note that if u is smooth on S^r , the derivative $P^{rr}(x)$ of the rth order stencil polynomial $P^r(x)$ is (r-1)st order accurate. Moreover, we wish to maintain spatial symmetry to avoid directional bias in the approximation of the diffusion operator. We therefore use a WENO-AO(4,3) reconstruction, which combines cubic and quadratic polynomials.

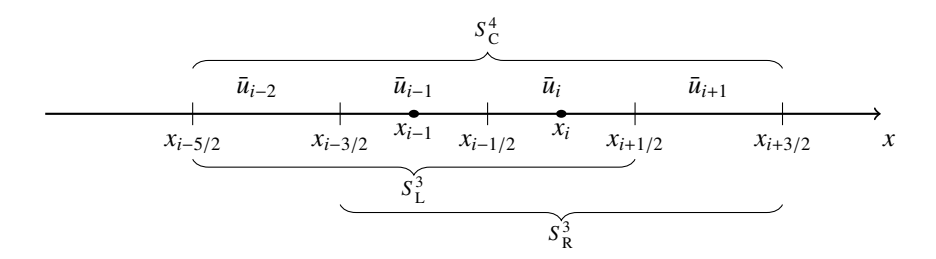


Figure 2.2: WENO-AO(4,3) stencils.

For a third order reconstruction of the derivative at $x = x_i$, we use the symmetric set of stencils shown in Figure 2.2. Reconstruct a fourth order stencil polynomial $P_{\rm C}^4$ over $S_{\rm C}^4 = \{I_{i-2}, I_{i-1}, I_i, I_{i+1}\}$, and two third order polynomials $P_{\rm L}^3$ and $P_{\rm R}^3$ over $S_{\rm L}^3 = \{I_{i-2}, I_{i-1}, I_i\}$ and $S_{\rm R}^3 = \{I_{i-1}, I_i, I_{i+1}\}$, respectively. Again, take any *linear weights* $\alpha_{\rm C}^4$, $\alpha_{\rm L}^3$, and $\alpha_{\rm R}^3$ arbitrarily as positive numbers summing up to one. (We take $\alpha_{\rm C}^4 = 1/2$ and $\alpha_{\rm L}^3 = \alpha_{\rm R}^3 = 1/4$.) Then the reconstruction of u_x at $x \in I_{i-1} \cup I_i$ is a convex combination of the three polynomials, defined as

$$u_{x}(x) \approx R_{i}^{\text{AO'}}(x) = \frac{\tilde{\alpha}_{\text{C}}^{4}}{\alpha_{\text{C}}^{4}} [P_{\text{C}}^{4\prime}(x) - \alpha_{\text{L}}^{3} P_{\text{L}}^{3\prime}(x) - \alpha_{\text{R}}^{3} P_{\text{R}}^{3\prime}(x)] + \tilde{\alpha}_{\text{L}}^{3} P_{\text{L}}^{3\prime}(x) + \tilde{\alpha}_{\text{R}}^{3} P_{\text{R}}^{3\prime}(x). \tag{2.4}$$

The *nonlinear weights* $\tilde{\alpha}_{\rm L}^4$, $\tilde{\alpha}_{\rm L}^3$, and $\tilde{\alpha}_{\rm R}^3$ are computed by (2.3), except that now $s \in \{3,4\}$. We may consider that x_i belongs to I_{i-1} or I_i , so we could define σ_{P^i} on either interval. We take the average of the two choices, and define

$$\sigma_{P^r} = \frac{1}{2} \sum_{i=i-1}^{i} \sum_{\ell=1}^{r-1} \int_{I_j} \Delta x_j^{2\ell-1} \left(\frac{d^{\ell}}{dx^{\ell}} P^r(x) \right)^2 dx.$$

The derivative is then approximated to third order when u is smooth on S_C^4 . Otherwise, we drop in order of accuracy when the solution is smooth on the center two cells $I_{i-1} \cup I_i$. As is usual in WENO methods, it is not so clear what

happens when the discontinuity is within $I_{i-1} \cup I_i$, i.e., no more than a cell away from x_i , although the reconstruction remains monotone [16] and we will see good numerical results later.

A more sophisticated procedure is needed if D = D(u) is not constant and may degenerate [17].

3. An adaptive Runge-Kutta method with backward Euler

For the time evolution, we choose to use a Runge-Kutta method, which could become unstable near discontinuities in the solution. We will develop a new method to improve stability near discontinuities when using a large timestep.

We recall the notation for such a Runge-Kutta method for systems of ordinary differential equations

$$v_t = g(v), \quad v(t_0) = v_0.$$
 (3.1)

An s-stage Runge-Kutta method for solving (3.1) is defined by an $s \times s$ matrix $\mathbf{A} = (a_{jm})$ and two s-vectors $\mathbf{c} = (c_j)$ and $\mathbf{b} = (b_j)$ with the standard assumptions $c_j = \sum_{m=1}^s a_{jm}$ and $\sum_{j=1}^s b_j = 1$. The method is

$$V^{n+c_j} = v^n + \Delta t_n \sum_{m=1}^s a_{jm} g(V^{n+c_m}), \quad 1 \le j \le s,$$
(3.2)

$$v^{n+1} = v^n + \Delta t_n \sum_{m=1}^s b_m \, g(V^{n+c_m}). \tag{3.3}$$

The Butcher tableau of the method is given in Table 3.1. A Runge-Kutta scheme is implicit if the matrix *A* has nonzero entries on or above the diagonal.

Table 3.1: Butcher tableau for (3.2)–(3.3).

To assess stability, let $k \in \mathbb{C}$ with Real(k) < 0 and consider the model problem

$$y'(t) = ky(t), \quad y(0) = 1.$$
 (3.4)

The Runge-Kutta method given by Table 3.1 applied to (3.4) is $y^{n+1} = \phi(z)y^n$, where the stability function is

$$\phi(z) = 1 + z\boldsymbol{b}^{T}(\boldsymbol{I} - z\boldsymbol{A})^{-1}\boldsymbol{e} = \frac{\det(\boldsymbol{I} - z\boldsymbol{A} + z\boldsymbol{e}\boldsymbol{b}^{T})}{\det(\boldsymbol{I} - z\boldsymbol{A})},$$

and where e denotes the vector of ones and $z = k\Delta t$. A Runge-Kutta method for solving (3.4) is unconditionally A-stable if $|\phi(z)| \le 1$. An L-stable method is A-stable and $|\phi(z)| \to 0$ as $|z| \to \infty$. L-stable methods work well for solving stiff problems, when Δt may be relatively large for some time scales.

3.1. An adaptive time integration

When there are discontinuities in the solution to (1.1), high order methods may generate oscillations even if they are L-stable. Strong stability preserving (SSP) Runge-Kutta methods guarantee the total variation diminishing (TVD) property under some time restrictions [4, 5, 6]. Unfortunately, there are no unconditionally SSP methods of order greater than one. In [21, 17], the authors compared a third order implicit SSP method with an L-stable method, and showed that, with a large timestep, the L-stable method has better results near discontinuities.

We want to take advantage of the unconditionally strong stability properties of the backward Euler method and its L-stability. Analogous to the WENO methodology, we consider an implicit scheme using a convex combination of a higher order and the backward Euler approximation of the time integration. Essentially, for (3.1) we want

$$v^{n+1} \stackrel{?}{=} \tilde{w}^{\text{High}} v^{n+1,\text{High}} + \tilde{w}^{\text{BE}} v^{n+1,\text{BE}},$$
 (3.5)

for some nonnegative *nonlinear* weights \tilde{w}^{High} and \tilde{w}^{BE} such that $\tilde{w}^{High} + \tilde{w}^{BE} = 1$. We will present later a way to make $\tilde{w}^{High} \approx 1$ when the solution is smooth, so that we achieve the accuracy of the high order Runge-Kutta method. However, when there are discontinuities in the solution, we will reduce the scheme to backward Euler, i.e., we will make $\tilde{w}^{BE} \approx 1$. This adaptive scheme should reduce oscillations in the solution.

We combine the high order s-stage Runge-Kutta method given by (3.2)–(3.3) (i.e., Table 3.1) with the composite backward Euler method computed using the same times t^{n+c_j} , $1 \le j \le s$. We must assume that the time levels satisfy $0 \le c_1 \le c_2 \le \cdots \le c_s = 1$. The Butcher tableau for this composite backward Euler method appears in Table 3.2, where $b_1^{\text{BE}} = c_1$ and $b_m^{\text{BE}} = c_m - c_{m-1}$, $2 \le m \le s$. Note that A^{BE} is defined by $a_{jm}^{\text{BE}} = b_m^{\text{BE}}$, $m \le j$, and $a_{jm}^{\text{BE}} = 0$ otherwise. The coefficients of the combined Runge-Kutta method are given by taking

$$\tilde{a}_{jm} = \tilde{w}^{\text{High}} a_{jm} + \tilde{w}^{\text{BE}} a_{jm}^{\text{BE}} \quad \text{and} \quad \tilde{b}_m = \tilde{w}^{\text{High}} b_m + \tilde{w}^{\text{BE}} b_m^{\text{BE}}. \tag{3.6}$$

Its Butcher tableau is the same as the one in Table 3.1, except that one should insert a tilde over each letter a and b.

Table 3.2: Butcher tableau for the composite backward Euler method, using the same times as the s-stage Runge-Kutta method of Table 3.1, where $b_1^{\rm BE}=c_1$ and $b_m^{\rm BE}=c_m-c_{m-1},\ 2\leq m\leq s$.

3.2. Application to the advection-diffusion equation

We apply the adaptive Runge-Kutta method (3.6) to (1.7). In order to maintain mass conservation in (1.1), we must use a flux-based approach discussed in [11]. We apply the time integration to each interface (at $x_{i-1/2}$ and $x_{i+1/2}$) rather than to each cell I_i , using the same Runge-Kutta method at $x_{i-1/2}$ for both I_{i-1} and I_i . In this way, the flux term $\hat{F}_{i-1/2}$ has a single value between these cells, regardless of whether we are solving for \bar{u}_{i-1} or \bar{u}_i , and thus mass is conserved in the overall scheme. Similarly, we use the same Runge-Kutta method at $x_{i+1/2}$ for both I_i and I_{i+1} . That is, a proper handling of the difference in flux values in (1.4) does not result in a straightforward application of (3.6) in the method of lines to (1.7) for each index i. Instead, we need to vary the combined Runge-Kutta coefficients from one interface point to the next. Therefore, we express (3.2)–(3.3), using the modified coefficients (3.6), applied to (1.7) as

$$\bar{U}_{i}^{n+c_{j}} = \bar{u}_{i}^{n} - \frac{\Delta t_{n}}{\Delta x_{i}} \sum_{m=1}^{s} \left[\tilde{a}_{jm,i+1/2} \hat{F}_{i+1/2}^{n+c_{m}} - \tilde{a}_{jm,i-1/2} \hat{F}_{i-1/2}^{n+c_{m}} \right], \quad 1 \le j \le s,$$
(3.7)

$$\bar{u}_i^{n+1} = \bar{u}_i^n - \frac{\Delta t_n}{\Delta x_i} \sum_{m=1}^s \left[\tilde{b}_{m,i+1/2} \hat{F}_{i+1/2}^{n+c_m} - \tilde{b}_{m,i-1/2} \hat{F}_{i-1/2}^{n+c_m} \right], \tag{3.8}$$

where $\hat{F}_{i\pm1/2}^{n+c_m} = \hat{F}(U_{i\pm1/2}^{n+c_m,-},U_{i\pm1/2}^{n+c_m,+},U_{x,i\pm1/2}^{n+c_m})$. We will see how to define the nonlinear weights in the next subsection.

3.3. The Third order Radau IIA method with backward Euler

To define a scheme that is third order accurate, we choose to use the 2-stage, L-stable, implicit Radau IIA Runge-Kutta method [22]. The Butcher tableau of this method, and the corresponding composite backward Euler method, is given in Table 3.3.

Table 3.3: Butcher tableau for the third order Radau IIA Runge-Kutta method (left) and the corresponding composite backward Euler method (right).

Our choice of third order scheme allows us to simplify (3.7)–(3.8). Because $b_j = a_{2j}$, we need not distinguish between \bar{u}_i^{n+1} and \bar{U}_i^{n+1} , and we can simply write $\bar{u}_i^{n+1/3} = \bar{U}_i^{n+1/3}$. Moreover, we can reduce the notation with $a^j = a_{1j}$ and $b^j = b_j = a_{2j}$. Rewriting (3.7)–(3.8), we have

$$\bar{u}_{i}^{n+1/3} = \bar{u}_{i}^{n} - \frac{\Delta t_{n}}{\Delta x_{i}} \left[\tilde{a}_{i+1/2}^{1} \hat{F}_{i+1/2}^{n+1/3} - \tilde{a}_{i-1/2}^{1} \hat{F}_{i-1/2}^{n+1/3} + \tilde{a}_{i+1/2}^{2} \hat{F}_{i+1/2}^{n+1} - \tilde{a}_{i-1/2}^{2} \hat{F}_{i-1/2}^{n+1} \right], \tag{3.9}$$

$$\bar{u}_{i}^{n+1} = \bar{u}_{i}^{n} - \frac{\Delta t_{n}}{\Delta x_{i}} \Big[\tilde{b}_{i+1/2}^{1} \hat{F}_{i+1/2}^{n+1/3} - \tilde{b}_{i-1/2}^{1} \hat{F}_{i-1/2}^{n+1/3} + \tilde{b}_{i+1/2}^{2} \hat{F}_{i+1/2}^{n+1} - \tilde{b}_{i-1/2}^{2} \hat{F}_{i-1/2}^{n+1} \Big], \tag{3.10}$$

where $\hat{F}_{i\pm1/2}^{n+\theta}=\hat{F}(u_{i\pm1/2}^{n+\theta,-},u_{i\pm1/2}^{n+\theta,+},u_{x,i\pm1/2}^{n+\theta}),\,\theta=1/3,1,$ and

$$\begin{split} \tilde{a}_{i\pm1/2}^{1} &= \frac{5}{12} \tilde{w}_{i\pm1/2}^{\text{Radau}} + \frac{1}{3} \tilde{w}_{i\pm1/2}^{\text{BE}}, \qquad \tilde{a}_{i\pm1/2}^{2} = -\frac{1}{12} \tilde{w}_{i\pm1/2}^{\text{Radau}}, \\ \tilde{b}_{i\pm1/2}^{1} &= \frac{3}{4} \tilde{w}_{i\pm1/2}^{\text{Radau}} + \frac{1}{3} \tilde{w}_{i\pm1/2}^{\text{BE}}, \qquad \tilde{b}_{i\pm1/2}^{2} = \frac{1}{4} \tilde{w}_{i\pm1/2}^{\text{Radau}} + \frac{2}{3} \tilde{w}_{i\pm1/2}^{\text{BE}}. \end{split}$$
(3.11)

Since the backward Euler method is globally first order accurate, to achieve the highest possible order in time (see Section 4), we need to scale the linear weight $w^{\rm BE}$ as $w^{\rm BE} = w_0^{\rm BE} \Delta t_n^2$ for some $w_0^{\rm BE} > 0$ (and $w_0^{\rm BE} \Delta t_n^2 < 1$), and then $w^{\rm Radau} = 1 - w^{\rm BE}$. The nonlinear weights are computed in the same way as in WENO spatial reconstruction, that is,

$$\hat{w}_{i\pm 1/2}^{\text{Radau}} = \frac{w^{\text{Radau}}}{(\epsilon_h + \sigma_{i\pm 1/2}^{\text{Radau}})^{\eta}}, \qquad \hat{w}_{i\pm 1/2}^{\text{BE}} = \frac{w^{\text{BE}}}{(\epsilon_h + \sigma^{\text{BE}})^{\eta}}, \tag{3.12}$$

where $\eta \ge 1$ and $\epsilon_h = \epsilon_0 h^2$, $\epsilon_0 > 0$, and the normalized nonlinear weights are

$$\tilde{w}_{i\pm 1/2}^{\text{Radau}} = \frac{\hat{w}_{i\pm 1/2}^{\text{Radau}}}{\hat{w}_{i\pm 1/2}^{\text{BE}} + \hat{w}_{i\pm 1/2}^{\text{Radau}}}, \qquad \tilde{w}_{i\pm 1/2}^{\text{BE}} = 1 - \tilde{w}_{i\pm 1/2}^{\text{Radau}}.$$
(3.13)

The smoothness indicators σ^{BE} and $\sigma^{Radau}_{i\pm 1/2}$ are used to detect a discontinuity or steep front in the solution. Recall that the smoothness indicator actually measures roughness (i.e., a larger value means a less smooth solution). For backward Euler, we simply take $\sigma^{BE}=0$, since it is always acceptable to use backward Euler. We define

$$\sigma^{\text{BE}} = 0, \tag{3.14}$$

$$\sigma_{i\pm 1/2}^{\text{Radau}} = (\bar{u}_{i\pm 1}^n - \bar{u}_i^n)^2 + (\bar{u}_{i\pm 1}^{n+1/3} - \bar{u}_i^{n+1/3})^2 + (\bar{u}_{i\pm 1}^{n+1} - \bar{u}_i^{n+1})^2. \tag{3.15}$$

The latter smoothness indicator, for Radau IIA, detects a shock in space. One can imagine using other possibilities, and we will consider some later in Section 6.

3.4. Solution by Newton's method

The overall scheme (3.9)–(3.10) is a coupled nonlinear system of equations. The nonlinearity is due to three sources. First, depending on the problem (1.1) solved, f and/or D may be nonlinear. This would cause the flux function $\hat{F}(u^-, u^+, u_x) = \hat{f}(u^-, u^+) - Du_x$ to be nonlinear through the Lax-Friedrichs flux $\hat{f}(1.5)$ and/or D(u). Second, the WENO-AO reconstructions appearing within the flux function are nonlinear with respect to the cell averages, due to the weighting procedure involving the smoothness indicator (2.1) and the normalization (2.3). Finally, a similar nonlinear weighting arises for the Runge-Kutta coefficients, due to the time adaptivity through the Radau smoothness indicator (3.15) (or any of those chosen in Section 6) and normalization (3.12)–(3.13).

In our numerical implementation, we solve the scheme (3.9)–(3.10) using a fairly straightforward application of Newton's method. The previous solution \bar{u}_i^n is used as the initial guess for both $\bar{u}_i^{n+1/3}$ and \bar{u}_i^{n+1} . At each Newton iteration, we solved for the update using a sparse direct solver, and we terminated the Newton iterations when the update was smaller than 1e-6 times one plus the initial residual. We tended to use about 4-5 iterations per time step, although very large CFL number problems may take up to about 15 iterations to converge.

The Jacobian matrix is sparse, with a structure that depends on the stencil of the WENO-AO reconstructions. Our third order scheme with Lax-Fredrich's stabilization (3.9)–(3.10) is a block 2×2 system for $\bar{u}_i^{n+1/3}$ and \bar{u}_i^{n+1} . In space, the WENO-AO(3,2) and WENO-AO(4,3) reconstructions for $u_{i\pm1/2}^{n+\theta,\pm}$ and $u_{x,i\pm1/2}^{n+\theta}$, $\theta=1/3,1$, involve $\bar{u}_j^{n+\theta}$ where j=i-2,i-1,i,i+1,i+2. In time, the smoothness indicators required to compute the adaptive Runge-Kutta coefficients $\tilde{a}_{i\pm1/2}^{\ell}$ and $\tilde{b}_{i\pm1/2}^{\ell}$, $\ell=1,2$, use only $\bar{u}_j^{n+1/3}$ and \bar{u}_j^{n+1} where j=i-1,i,i+1. Therefore the system is block structured with 5 bands. This would imply an overall band structure of 11 individual bands (i.e., 5 block 2×2 bands are 11 individual bands, since the 2×2 center block adds one band to the right for the first equation and one to the left for the second equation).

The most difficult part of the Jacobian matrix to compute is related to the derivatives of the spatial WENO-AO reconstructions. However, as discussed in [23, 17], this is facilitated by defining the base polynomials. Briefly, given a stencil S of contiguous mesh cells I_k , let ψ_k be the polynomial such that

$$\frac{1}{\Delta x_{\ell}} \int_{I_{\ell}} \psi_k(x) \, dx = \begin{cases} 1, & \ell = k, \\ 0, & \text{otherwise,} \end{cases} \quad \forall I_{\ell} \in S.$$

In fact, these can be precomputed once the mesh is given. The stencil polynomial is then

$$P(x) = \sum_{k} \bar{u}_k \psi_k(x), \quad \forall I_k \in S.$$
 (3.16)

That is, the derivative $\partial P/\partial \bar{u}_k$ in the Jacobian is simply ψ_k . Moreover, using (3.16), the smoothness indicator for the cell I_i is

$$\sigma_{P} = \sum_{\ell=1}^{r} \int_{I_{i}} \Delta x_{i}^{2\ell-1} \left(\frac{d^{\ell} P}{dx^{\ell}}\right)^{2} dx = \sum_{j} \sum_{k} \bar{u}_{j} \bar{u}_{k} \left(\sum_{\ell=1}^{r} \int_{I_{i}} \Delta x_{i}^{2\ell-1} \frac{d^{\ell} \psi_{j}}{dx^{\ell}} \frac{d^{\ell} \psi_{k}}{dx^{\ell}} dx\right) = \sum_{j} \sum_{k} \bar{u}_{j} \bar{u}_{k} \, \sigma_{jk}^{i}, \tag{3.17}$$

where σ^i_{jk} can be precomputed from the computational mesh. It is also the derivative $\sigma^i_{jk} = \partial \sigma_P / \partial \bar{u}_j = \partial \sigma_P / \partial \bar{u}_k$ needed in the Jacobian.

4. Analysis of time discretization errors

In this section, we analyze our new third order scheme (3.9)–(3.10) in two cases: when the solution is smooth, and when it has a discontinuity. We assume in this section that $\Delta t = C_0 h$, for some $C_0 > 0$, to balance the spatial and temporal errors arising in the hyperbolic part of the equation (1.1). Recall that $\sigma^{\text{BE}} = 0$, $w^{\text{BE}} = w_0^{\text{BE}} \Delta t_n^2 = O(h^2)$, $w^{\text{Radau}} = 1 - w^{\text{BE}}$, and $\epsilon_h = \epsilon_0 h^2$. Define

$$\tau_{i\pm 1/2} = \left(\frac{\epsilon_h}{\epsilon_h + \sigma_{i\pm 1/2}^{\text{Radau}}}\right)^{\eta} = \left(\frac{\epsilon_0 h^2}{\epsilon_0 h^2 + \sigma_{i\pm 1/2}^{\text{Radau}}}\right)^{\eta},\tag{4.1}$$

so that

$$\tilde{w}_{i\pm 1/2}^{\text{Radau}} = \frac{w^{\text{Radau}}}{w^{\text{Radau}} + w^{\text{BE}} \tau_{i\pm 1/2}^{-1}} = \frac{1 - w_0^{\text{BE}} \Delta t_n^2}{1 + w_0^{\text{BE}} \Delta t_n^2 (\tau_{i\pm 1/2}^{-1} - 1)}$$
(4.2)

and

$$\tilde{w}_{i\pm 1/2}^{\text{BE}} = \frac{w^{\text{BE}}}{w^{\text{BE}} + w^{\text{Radau}} \tau_{i\pm 1/2}} = \frac{w_0^{\text{BE}} \Delta t_n^2}{w_0^{\text{BE}} \Delta t_n^2 + (1 - w_0^{\text{BE}} \Delta t_n^2) \tau_{i\pm 1/2}}.$$
(4.3)

4.1. The smooth case

When the solution is smooth, $\sigma^{\text{Radau}}_{i\pm 1/2} = O(h^2)$, and so we conclude from (4.1) that $\tau_{i\pm 1/2} = \Theta(1)$, and then from (4.3) that $\tilde{w}^{\text{BE}}_{i\pm 1/2} = O(h^2)$. Recall that $g(h) = \Theta(h^p)$ means that there are constants c > 0 and c > 0 such that $ch^p \le |g(h)| \le Ch^p$ as $h \to 0$; whereas, $g(h) = O(h^p)$ means only that $|g(h)| \le Ch^p$ as $h \to 0$.

Note that the Runge-Kutta coefficients (3.11) can be rewritten as

$$\tilde{a}_{i\pm 1/2}^{1} = \frac{5}{12} - \frac{1}{12} \tilde{w}_{i\pm 1/2}^{\text{BE}}, \qquad \tilde{a}_{i\pm 1/2}^{2} = -\frac{1}{12} + \frac{1}{12} \tilde{w}_{i\pm 1/2}^{\text{BE}},$$

$$\tilde{b}_{i\pm 1/2}^{1} = \frac{3}{4} - \frac{5}{12} \tilde{w}_{i\pm 1/2}^{\text{BE}}, \qquad \tilde{b}_{i\pm 1/2}^{2} = \frac{1}{4} + \frac{5}{12} \tilde{w}_{i\pm 1/2}^{\text{BE}}.$$

$$(4.4)$$

That is, the adaptive Runge-Kutta method is a simple perturbation of order $\tilde{w}_{i\pm 1/2}^{\rm BE} = O(h^2)$ of the Radau IIA Runge-Kutta method. If we can show that this perturbation is on the same order as the local truncation error of Radau IIA (i.e., $O(h^4)$), then the adaptive method retains the third order global accuracy. To be more precise, our adaptive Runge-Kutta scheme (3.9)–(3.10) can be written as the Radau IIA Runge-Kutta scheme (using the Butcher Tableau on the left of Table 3.3) plus a perturbation, namely,

$$\bar{u}_{i}^{n+1/3} = \bar{u}_{i}^{n} - \frac{\Delta t_{n}}{\Delta x_{i}} \left[\frac{5}{12} \hat{F}_{i+1/2}^{n+1/3} - \frac{5}{12} \hat{F}_{i-1/2}^{n+1/3} - \frac{1}{12} \hat{F}_{i+1/2}^{n+1} + \frac{1}{12} \hat{F}_{i-1/2}^{n+1} \right] + \frac{\Delta t_{n}}{12\Delta x_{i}} E_{i}, \tag{4.5}$$

$$\bar{u}_{i}^{n+1} = \bar{u}_{i}^{n} - \frac{\Delta t_{n}}{\Delta x_{i}} \left[\frac{3}{4} \hat{F}_{i+1/2}^{n+1/3} - \frac{3}{4} \hat{F}_{i-1/2}^{n+1/3} + \frac{1}{4} \hat{F}_{i+1/2}^{n+1} - \frac{1}{4} \hat{F}_{i-1/2}^{n+1} \right] + \frac{5\Delta t_{n}}{12\Delta x_{i}} E_{i}, \tag{4.6}$$

where the perturbation is a multiple of

$$E_i = \tilde{w}_{i+1/2}^{\mathrm{BE}} \hat{F}_{i+1/2}^{n+1/3} - \tilde{w}_{i-1/2}^{\mathrm{BE}} \hat{F}_{i-1/2}^{n+1/3} - \tilde{w}_{i+1/2}^{\mathrm{BE}} \hat{F}_{i+1/2}^{n+1} + \tilde{w}_{i-1/2}^{\mathrm{BE}} \hat{F}_{i-1/2}^{n+1}$$

We wish to show that the local truncation error of (4.5)–(4.6) is $O(h^4)$, and this holds provided it holds for the perturbation terms.

Now

$$E_{i} = \tilde{w}_{i+1/2}^{\text{BE}} (\hat{F}_{i+1/2}^{n+1/3} - \hat{F}_{i-1/2}^{n+1/3} - \hat{F}_{i+1/2}^{n+1} + \hat{F}_{i-1/2}^{n+1}) - (\tilde{w}_{i+1/2}^{\text{BE}} - \tilde{w}_{i-1/2}^{\text{BE}})(\hat{F}_{i-1/2}^{n+1} - \hat{F}_{i-1/2}^{n+1/3})$$

$$= \tilde{w}_{i+1/2}^{\text{BE}} O(h^{2}) + (\tilde{w}_{i+1/2}^{\text{BE}} - \tilde{w}_{i-1/2}^{\text{BE}})O(h),$$

using Taylor expansions and our assumption that $\Delta t = O(h)$. Now from (4.3)

$$\tilde{w}_{i+1/2}^{\text{BE}} - \tilde{w}_{i-1/2}^{\text{BE}} = \frac{w_0^{\text{BE}} \Delta t_n^2}{w_0^{\text{BE}} \Delta t_n^2 + (1 - w_0^{\text{BE}} \Delta t_n^2) \tau_{i+1/2}} - \frac{w_0^{\text{BE}} \Delta t_n^2}{w_0^{\text{BE}} \Delta t_n^2 + (1 - w_0^{\text{BE}} \Delta t_n^2) \tau_{i-1/2}}$$
$$= O(\Delta t_n^2 (\tau_{i+1/2} - \tau_{i-1/2})).$$

Given $\varphi(\sigma) = \left(\frac{\epsilon_0 h^2}{\epsilon_0 h^2 + \sigma}\right)^{\eta}$ and $\eta \ge 1$, we have from (4.1) that

$$\tau_{i+1/2} - \tau_{i-1/2} = \varphi(\sigma_{i+1/2}^{\text{Radau}}) - \varphi(\sigma_{i-1/2}^{\text{Radau}}) = \varphi'(\sigma) \left(\sigma_{i+1/2}^{\text{Radau}} - \sigma_{i-1/2}^{\text{Radau}}\right),$$

where σ is between $\sigma_{i+1/2}^{\text{Radau}}$ and $\sigma_{i-1/2}^{\text{Radau}}$, and all these quantities are $O(h^2)$. Since $\varphi'(\sigma) = -\eta \frac{\varphi(\sigma)}{\epsilon_0 h^2 + \sigma}$, we have that

$$|\tau_{i+1/2} - \tau_{i-1/2}| = \left| \eta \left(\frac{\epsilon_0 h^2}{\epsilon_0 h^2 + \sigma} \right)^{\eta} \frac{\sigma_{i+1/2}^{\text{Radau}} - \sigma_{i-1/2}^{\text{Radau}}}{\epsilon_0 h^2 + \sigma} \right| \leq C \left| \frac{\sigma_{i+1/2}^{\text{Radau}} - \sigma_{i-1/2}^{\text{Radau}}}{h^2} \right|$$

Recall (3.15), the definition of σ^{Radau} , and note that

$$(\bar{u}_{i+1} - \bar{u}_i)^2 - (\bar{u}_i - \bar{u}_{i-1})^2 = (\bar{u}_{i+1} - \bar{u}_{i-1})(\bar{u}_{i+1} - 2\bar{u}_i + \bar{u}_{i-1}) = O(h^3),$$

to conclude that $\sigma_{i+1/2}^{\text{Radau}} - \sigma_{i-1/2}^{\text{Radau}} = O(h^3)$. Therefore $\tau_{i+1/2} - \tau_{i-1/2} = O(h)$, $\tilde{w}_{i+1/2}^{\text{BE}} - \tilde{w}_{i-1/2}^{\text{BE}} = O(h^3)$, and, finally, $E_i = O(h^4)$, as desired.

As the Radau IIA scheme is locally fourth order accurate, the adaptive scheme is also locally fourth order accurate. We have established that the adaptive scheme is globally third order accurate when *u* is smooth.

4.2. The case of a discontinuity

Now consider the case in which the solution u has a discontinuity. Backward Euler is globally at least $O(h^{1/2})$ in the presence of a discontinuity [24, 25], which means that it should have local truncation error at least $O(h^{3/2})$. So we would like to see that our method has a local truncation error of at least $O(h^{3/2})$. We assume that the solution is smooth on $(-\infty, x_{j-1/2}) \cup (x_{k+1/2}, \infty) \times [t^n, t^{n+1}]$ and has a shock traveling through the cells $\{I_j, \dots, I_k\}$ for some j, $k \in \mathbb{N}$. We describe the cells I_{j-1} and I_{k+1} as transition cells, i.e., cells in which one interface has a Radau weight $\tilde{w}_{i+1/2}^{\text{Radau}} = 1 - O(h^2)$ and the other interface has $\tilde{w}_{i+1/2}^{\text{Radau}} = \Theta(h^{2\eta-2})$. A shock cell will be a cell between the transition cells which has Radau weights $\tilde{w}_{i+1/2}^{\text{Radau}} = \Theta(h^{2\eta-2})$ for both the right and left interfaces. Finally, smooth cells are those outside of $\{I_j, \dots, I_{k+1}\}$. These cells are not effected by the shock and thus have Radau weights $\tilde{w}_{i\pm 1/2}^{\text{Radau}} = 1 - O(h^2)$ for both interfaces.

We now write the adaptive Runge-Kutta coefficients (3.11) as a perturbation of the backward Euler method:

$$\tilde{a}_{i\pm 1/2}^{1} = \frac{1}{3} + \frac{1}{12} \tilde{w}_{i\pm 1/2}^{\text{Radau}}, \qquad \tilde{a}_{i\pm 1/2}^{2} = -\frac{1}{12} \tilde{w}_{i\pm 1/2}^{\text{Radau}},$$

$$\tilde{b}_{i\pm 1/2}^{1} = \frac{1}{3} + \frac{5}{12} \tilde{w}_{i\pm 1/2}^{\text{Radau}}, \qquad \tilde{b}_{i\pm 1/2}^{2} = \frac{2}{3} - \frac{5}{12} \tilde{w}_{i\pm 1/2}^{\text{Radau}}.$$

$$(4.7)$$

In analogy to (4.5)–(4.6), our adaptive scheme is the backward Euler scheme plus a perturbation, which is a multiple

$$E_{i} = \tilde{w}_{i+1/2}^{\text{Radau}} \hat{F}_{i+1/2}^{n+1/3} - \tilde{w}_{i-1/2}^{\text{Radau}} \hat{F}_{i-1/2}^{n+1/3} - \tilde{w}_{i+1/2}^{\text{Radau}} \hat{F}_{i+1/2}^{n+1} + \tilde{w}_{i-1/2}^{\text{Radau}} \hat{F}_{i-1/2}^{n+1}.$$

$$(4.8)$$

In fact, the perturbation is $(\Delta t_n/\Delta x_i)E_i/12$ and $(\Delta t_n/\Delta x_i)5E_i/12$ for (3.9) and (3.10), respectively.

The order of accuracy of the perturbation depends on which classification the cell I_i belongs, i.e., transition, shock, or smooth. For the latter two cases (shock and smooth cells), note that (4.8) becomes

$$E_{i} = \tilde{w}_{i+1/2}^{\text{Radau}} (\hat{F}_{i+1/2}^{n+1/3} - \hat{F}_{i-1/2}^{n+1/3} - \hat{F}_{i+1/2}^{n+1} + \hat{F}_{i-1/2}^{n+1}) + (\tilde{w}_{i+1/2}^{\text{Radau}} - \tilde{w}_{i-1/2}^{\text{Radau}}) (\hat{F}_{i-1/2}^{n+1/3} - \hat{F}_{i-1/2}^{n+1}). \tag{4.9}$$

Let I_i be a smooth cell, that is, I_i does not see the shock. To determine the order of the perturbation in I_i first observe that

$$\tilde{w}_{i+1/2}^{\mathrm{Radau}} - \tilde{w}_{i-1/2}^{\mathrm{Radau}} = \tilde{w}_{i-1/2}^{\mathrm{BE}} - \tilde{w}_{i+1/2}^{\mathrm{BE}} = O(h^3)$$

by Section 4.1. Hence,

$$E_i = O(h^2) + O(h^3)O(h) = O(h^2)$$

by Taylor expansions and using that $\tilde{w}_{i\pm 1/2}^{\rm Radau} = \Theta(1)$. Now let I_i be a shock cell, so that $\sigma_{i\pm 1/2}^{\rm Radau} = 1 - O(h^2)$. We conclude from (4.1) that $\tau_{i\pm 1/2} = \Theta(h^{2\eta})$ and then from (4.2) that $\tilde{w}_{i\pm 1/2}^{\rm Radau} = \Theta(h^{2\eta-2})$. So, the perturbation (4.9) in the shock cell is

$$E_i = \tilde{w}_{i+1/2}^{\text{Radau}} O(1) + (\tilde{w}_{i+1/2}^{\text{Radau}} - \tilde{w}_{i-1/2}^{\text{Radau}}) O(1) = O(h^{2\eta-2}),$$

where we again used that $\tilde{w}_{i+1/2}^{\text{Radau}} - \tilde{w}_{i-1/2}^{\text{Radau}} = \tilde{w}_{i-1/2}^{\text{BE}} - \tilde{w}_{i+1/2}^{\text{BE}}$, and we repeated the argument given in Section 4.1 except with $\sigma_{i-1/2}^{\text{Radau}} - \sigma_{i+1/2}^{\text{Radau}} = O(1)$ and $\sigma = \Theta(1)$.

Finally, let I_i be a transition cell, that is, only one interface sees the shock. Without loss of generality, assume that the shock crosses the right interface of the cell so that the Radau weight is $\tilde{w}_{i+1/2}^{\text{Radau}} = \Theta(h^{2\eta-2})$. Moreover the left interface has a Radau weight $\tilde{w}_{i-1/2}^{\text{Radau}} = \Theta(1)$. Then (4.8) becomes

$$\begin{split} E_i &= \tilde{w}_{i+1/2}^{\text{Radau}}(\hat{F}_{i+1/2}^{n+1/3} - \hat{F}_{i+1/2}^{n+1}) - \tilde{w}_{i-1/2}^{\text{Radau}}(\hat{F}_{i-1/2}^{n+1/3} - \hat{F}_{i-1/2}^{n+1}) \\ &= \Theta(h^{2\eta-2})O(1) - \Theta(1)O(h), \\ &= O(h) \end{split}$$

because the solution is smooth at $x_{i-1/2}$, i.e., $\hat{F}_{i-1/2}^{n+1/3} - \hat{F}_{i-1/2}^{n+1} = O(h)$.

To summarize, we have that the perturbation has an order of accuracy of $O(h^2)$, $O(h^{2\eta-2})$, and O(h) in the smooth, shock, and transition cells, respectively. We conclude that the adaptive Runge-Kutta method has an overall perturbation of order $O(h^{\min(2,2\eta-2,1)}) = O(h)$ (since $\eta \ge 3/2$) of the backward Euler method when the solution has a discontinuity, which is similar to what has been observed for flux-based partitioned Runge-Kutta methods [9, 14, 11]. But this is less than the desired $O(h^{3/2})$ and would suggest that the global error is O(1). (We remark that a similar analysis of the backward Euler method would suggest that it has a local truncation error of only O(h) as well!) In fact, there are very few transition cells, and each is only of width h, so in an L^1 norm, we should expect that they do not degrade the overall accuracy (provided $\eta \ge 7/4$). The numerical results of the next subsection suggest that this is indeed the case.

4.3. Numerical convergence

We test the convergence rate of our numerical scheme on the nonlinear Burgers equation with a simple initial condition; that is, for the problem

$$u_t + (u^2/2)_x = 0, \quad x \in (0, 2),$$
 (4.10)

with the initial condition (IC)

$$u_0(x) = 0.5 - 0.25\sin(\pi x).$$
 (4.11)

The test uses a uniform grid with m elements, $\Delta x_i = h$, $\epsilon = h^2$, and $\eta = 2$.

We ran the computation over gradually refined meshes up to time t=1, before shocks develop. The numerical errors and convergence orders for the adaptive scheme are given in Table 4.1 using various CFL numbers with $w^{\rm BE}=\Delta t^2$. We see third order convergence in both the discrete L^1 and L^∞ norms, which is consistent with the theory in Section 4.1.

$\begin{array}{c ccccccccccccccccccccccccccccccccccc$							
$ \begin{array}{c ccccccccccccccccccccccccccccccccccc$		L_h^1		L_h^{∞}			
$\begin{array}{c ccccccccccccccccccccccccccccccccccc$	m	error	order	error	order		
$\begin{array}{c ccccccccccccccccccccccccccccccccccc$			$\Delta t = h$				
$\begin{array}{c ccccccccccccccccccccccccccccccccccc$	640	3.21E-06	2.93	4.28E-05	2.87		
$\begin{array}{c ccccccccccccccccccccccccccccccccccc$	1280	4.05E-07	2.99	5.47E-06	2.97		
1280 1.86E-04 2.29 2.81E-03 1.92 2560 2.86E-05 2.70 4.84E-04 2.54 5120 3.78E-06 2.92 6.57E-05 2.88 Δt = 50h 5120 3.09E-04 2.06 4.39E-03 1.67 10240 5.12E-05 2.59 8.45E-04 2.38	2560	5.07E-08	3.00	6.87E-07	2.99		
2560 2.86E-05 2.70 4.84E-04 2.54 5120 3.78E-06 2.92 6.57E-05 2.88 Δt = 50h 5120 3.09E-04 2.06 4.39E-03 1.67 10240 5.12E-05 2.59 8.45E-04 2.38			$\Delta t = 10h$				
5120 $3.78\text{E-}06$ 2.92 $6.57\text{E-}05$ 2.88 $\Delta t = 50h$ 5120 $3.09\text{E-}04$ 2.06 $4.39\text{E-}03$ 1.67 10240 $5.12\text{E-}05$ 2.59 $8.45\text{E-}04$ 2.38	1280	1.86E-04	2.29	2.81E-03	1.92		
$ \begin{array}{c ccccccccccccccccccccccccccccccccccc$	2560	2.86E-05	2.70	4.84E-04	2.54		
5120 3.09E-04 2.06 4.39E-03 1.67 10240 5.12E-05 2.59 8.45E-04 2.38	5120	3.78E-06	2.92	6.57E-05	2.88		
10240 5.12E-05 2.59 8.45E-04 2.38	$\Delta t = 50h$						
	5120	3.09E-04	2.06	4.39E-03	1.67		
20480 7.13E-06 2.85 1.23E-04 2.78	10240	5.12E-05	2.59	8.45E-04	2.38		
	20480	7.13E-06	2.85	1.23E-04	2.78		

Table 4.1: Burgers equation (4.10) with IC (4.11), before the shock develops. Error and convergence order at t = 1.

Next we test the convergence rate by fixing w^{BE} at each gridpoint. The results are shown in Fig. 4.1. We first take $w^{BE} = 0$ at x_i when i is even and $w^{BE} = 1$ at x_i when i is odd. Hence, in the context of Section 4.2, we are choosing to make every cell a transition cell. We see O(h) order of convergence (circles) which supports our contention that the transition cells do not degrade the overall accuracy. However, if we take $w^{BE} = 1$ at $x_{m/2}$ and $w^{BE} = 0$ at all other gridpoints, second order convergence is observed (squares). This is also consistent with our contention that the transition cells do not degrade the overall accuracy very much, and that their influence is proportional to h when discontinuities in the solution are isolated. We also show the convergence of the Radau IIA method, that is, using $w^{BE} = 0$ at all gridpoints, which achieves the optimal third order accuracy for this smooth problem.

Now we take the final time t=2 after the shock has developed. Table 4.2 shows the third order convergence on $[0.2, 0.6] \cup [1.4, 1.8]$ where the solution is smooth using $\Delta t = 3h$ and $\Delta t = 5h$.

We finally take the step function

$$u(x,0) = \begin{cases} a & x < 0.5, \\ b & x > 0.5, \end{cases}$$
 (4.12)

as the initial condition with a = 1 and b = 0. The shock travels with speed 1/2. Table 4.3 shows that the convergence rate of all three schemes is first order. Section 4.2 showed that the adaptive Runge-Kutta method is a perturbation of the backward Euler method which should not reduce the overall order of accuracy in the presence of a discontinuity. In theory, the local truncation error of backward Euler for discontinuous solutions is $O(h^{1/2})$ [24, 25]; however, in

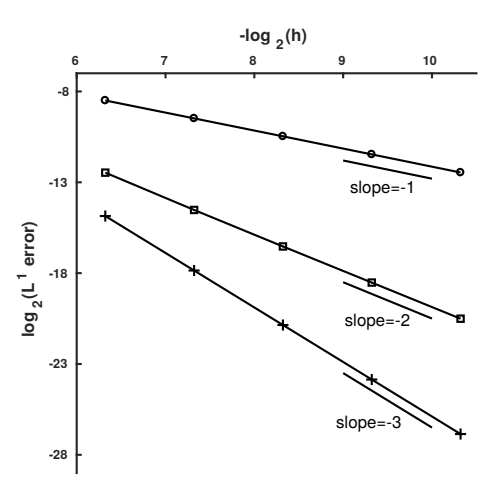


Figure 4.1: Burgers equation (4.10) with IC (4.11) before shocks develop. Error and convergence order at t = 0.5 with $\Delta t = h$. Circles are the results using alternating values of w^{BE} . Squares are the results using $w^{\text{BE}} = 0$ except at $x_{m/2}$. The '+' signs are the results using $w^{\text{BE}} = 0$ for all gridpoints.

	$\Delta t = 3h$				$\Delta t = 5h$			
	L_h^1		L_h^{∞}		L_h^1		L_h^{∞}	
m	error	order	error	order	error	order	error	order
160	8.23E-06	2.92	1.78E-05	2.95	3.93E-05	2.85	8.20E-05	2.87
320	1.05E-06	2.97	2.25E-06	2.98	5.07E-06	2.96	1.05E-05	2.97
640	1.32E-07	2.99	2.82E-07	2.99	6.40E-07	2.98	1.32E-06	2.99

Table 4.2: Burgers equation (4.10) with IC (4.11) after shocks develop. Error and convergence order at t = 2 on $[0.2, 0.6] \cup [1.4, 1.8]$, which avoids the shock.

practice the error tends to behave more like O(h) (see, e.g., [16]), and we see this same order of accuracy for our adaptive scheme.

5. Von Neumann stability analysis

We analyze the constant coefficient linear advection-diffusion equation

$$u_t + au_x - Du_{xx} = 0, \quad x \in \mathbb{R}, \ t > 0,$$
 (5.1)

where a > 0 and $D \ge 0$. In this section, we will also assume that we use a uniform grid, so $\Delta x_i = h$, for all j.

We apply the von Neumann stability analysis (see, e.g., [26]) to show that the linear scheme is L-stable for smooth solutions. Consider the kth single Fourier mode $\bar{u}(x,t) = T(t)e^{ikx}$, where in this section i is the canonical imaginary root of -1. Without loss of generality, assume $x_0 = 0$, so $x_i = jh$. Then

$$\bar{u}_j(t) = T(t)e^{ikx_j} = T(t)e^{ikjh} = T(t)e^{ij\theta}, \tag{5.2}$$

where $\theta = kh$. We want to show that $\frac{|T^{n+1}|}{|T^n|} \le 1$ and $\lim_{\Delta t \to \infty} \frac{|T^{n+1}|}{|T^n|} \to 0$. In terms of (5.2), the kth single Fourier mode at our three time levels are

$$\bar{u}_{j}^{n} = T^{n} e^{ij\theta}, \quad \bar{u}_{j}^{n+1/3} = T^{n+1/3} e^{ij\theta}, \quad \text{and} \quad \bar{u}_{j}^{n+1} = T^{n+1} e^{ij\theta}.$$

We assume that the solution u is smooth. WENO methodology then implies that all the nonlinear weights are approximately equal to the linear weights. That is, in space, $\tilde{\alpha}_j \approx \alpha_j$ for all j, and in time, $\tilde{w}_{j+1/2}^{\rm BE} = \tilde{w}_{j-1/2}^{\rm BE} \approx w^{\rm BE} = w$, $w \ge 0$, and $\tilde{w}_{j+1/2}^{\rm Radau} = \tilde{w}_{j-1/2}^{\rm Radau} \approx 1 - w^{\rm BE} = 1 - w$. The Butcher tableau for this Runge-Kutta method is given in Table 5.1.

	$\Delta t = 2h$		$\Delta t = 10h$		$\Delta t = 14h$			
	L_h^1		L_h^1		L_h^1			
m	error	order	error	order	error	order		
			BE					
160	1.04E-02	0.98	2.73E-02	0.98	3.15E-02	1.05		
320	5.22E-03	0.99	1.37E-02	0.99	1.47E-02	1.10		
640	2.62E-03	1.00	6.86E-03	1.00	8.59E-03	0.77		
		Radau						
160	7.27E-03	1.00	1.70E-02	1.00	1.97E-02	1.03		
320	3.64E-03	1.00	8.47E-03	1.00	8.52E-03	1.21		
640	1.82E-03	1.00	4.23E-03	1.00	5.14E-03	0.73		
	Radau + BE							
160	1.03E-02	0.98	2.71E-02	0.97	3.13E-02	1.06		
320	5.19E-03	0.99	1.36E-02	0.99	1.45E-02	1.11		
640	2.60E-03	0.99	6.83E-03	1.00	8.56E-03	0.76		

Table 4.3: Burgers equation (4.10) with Riemann IC (4.12), a shock moving with speed 1/2. Error and convergence order at t = 1 for backward Euler (BE), Radau IIA, and the adaptive procedure.

Table 5.1: Butcher tableau for the third order Radau IIA adaptive method with BE for smooth u.

Because the WENO nonlinear weights reduce to the linear ones, the reconstruction of the left point value at $x_{j-1/2} \in I_{j-1}$ is

$$u_{j-1/2}^{-}(t) = R_{j-1}(x_{j-1/2};t) = P_{\mathcal{C}}^{3}(x_{j-1/2}) = \frac{1}{6}(-\bar{u}_{j-2} + 5\bar{u}_{j-1} + 2\bar{u}_{j}),$$

and, from (2.4),

$$u_{x,j-1/2} = R_j^{\text{AO}\prime}(x_{j-1/2},t) = P_{\text{C}}^{4\prime}(x_{j-1/2}) = \frac{1}{12h}(\bar{u}_{j-2} - 15\bar{u}_{j-1} + 15\bar{u}_j - \bar{u}_{j+1}).$$

The numerical flux terms are

$$\begin{split} \hat{f}_{j+1/2} - \hat{f}_{j-1/2} &= \frac{a}{6} \big[(-\bar{u}_{j-1} + 5\bar{u}_j + 2\bar{u}_{j+1}) - (-\bar{u}_{j-2} + 5\bar{u}_{j-1} + 2\bar{u}_j) \big] \\ &= \frac{a}{6} \big[\bar{u}_{j-2} - 6\bar{u}_{j-1} + 3\bar{u}_j + 2\bar{u}_{j+1}) \big] \\ &= \frac{a}{6} T(t) e^{ij\theta} \big[e^{-2i\theta} - 6e^{-i\theta} + 3 + 2e^{i\theta} \big], \end{split}$$

using (5.2) at the fixed time t. Moreover

$$e^{-2i\theta} - 6e^{-i\theta} + 3 + 2e^{i\theta} = (\cos\theta - i\sin\theta)^2 - 6(\cos\theta - i\sin\theta) + 3 + 2(\cos\theta + i\sin\theta)$$

$$= \cos^2\theta - \sin^2\theta - 2i\cos\theta\sin\theta + 3 - 4\cos\theta + 8i\sin\theta$$

$$= 2 - 4\cos\theta + 2\cos^2\theta + 2i\sin\theta(4 - \cos\theta)$$

$$= 2(1 - \cos\theta)^2 + 2i\sin\theta(4 - \cos\theta),$$

which has nonnegative real part. The numerical diffusion terms are

$$\begin{split} -(\hat{h}_{j+1/2} - \hat{h}_{j-1/2}) &= -\frac{D}{12h} \big[(\bar{u}_{j-1} - 15\bar{u}_j + 15\bar{u}_{j+1} - \bar{u}_{j+2}) - (\bar{u}_{j-2} - 15\bar{u}_{j-1} + 15\bar{u}_j - \bar{u}_{j+1}) \big] \\ &= \frac{D}{12h} \big[\bar{u}_{j-2} - 16\bar{u}_{j-1} + 30\bar{u}_j - 16\bar{u}_{j+1} + \bar{u}_{j+2} \big] \\ &= \frac{D}{12h} T(t) e^{ij\theta} \big[e^{-2i\theta} - 16e^{-i\theta} + 30 - 16e^{i\theta} + e^{2i\theta} \big], \end{split}$$

and

$$e^{-2i\theta} - 16e^{-i\theta} + 30 - 16e^{i\theta} + e^{2i\theta}$$

$$= (\cos \theta - i\sin \theta)^2 - 16(\cos \theta - i\sin \theta) + 30 - 16(\cos \theta + i\sin \theta) + (\cos \theta + i\sin \theta)^2$$

$$= 30 - 32\cos \theta + 2(\cos^2 \theta - \sin^2 \theta)$$

$$= 4(1 - \cos \theta)(7 - \cos \theta),$$

which is nonnegative. Therefore, the number

$$\zeta = T(t)^{-1} e^{-ij\theta} \frac{\Delta t_n}{h} \left[(\hat{f}_{j+1/2} - \hat{f}_{j-1/2}) - (\hat{h}_{j+1/2} - \hat{h}_{j-1/2}) \right]$$

$$= \frac{\Delta t_n}{h} \left\{ \frac{a}{3} \left[(1 - \cos\theta)^2 + i\sin\theta \left(4 - \cos\theta \right) \right] + \frac{D}{3h} (1 - \cos\theta) (7 - \cos\theta) \right\}$$
(5.3)

is complex and has nonnegative real part.

Substituting the above results into (3.9)–(3.10) and using Table 5.1, we have that

$$T^{n+1/3} - T^n + \left[\left(\frac{5}{12} - \frac{1}{12} w \right) T^{n+1/3} + \left(-\frac{1}{12} + \frac{1}{12} w \right) T^{n+1} \right] \zeta = 0,$$

$$T^{n+1} - T^n + \left[\left(\frac{3}{4} - \frac{5}{12} w \right) T^{n+1/3} + \left(\frac{1}{4} + \frac{5}{12} w \right) T^{n+1} \right] \zeta = 0,$$

and in the matrix form,

$$\begin{bmatrix} 12 + (5-w)\zeta & (-1+w)\zeta \\ (9-5w)\zeta & 12 + (3+5w)\zeta \end{bmatrix} \begin{bmatrix} T^{n+1/3} \\ T^{n+1} \end{bmatrix} = T^n \begin{bmatrix} 12 \\ 12 \end{bmatrix}.$$

Hence, after inverting the 2×2 matrix,

$$T^{n+1} = \frac{12[(-9+5w)\zeta+12+(5-w)\zeta]}{[12+(5-w)\zeta][12+(3+5w)\zeta]+(1-w)(9-5w)\zeta^2}$$
$$= \frac{18+6(-1+w)\zeta}{18+6(2+w)\zeta+(3+w)\zeta^2}$$
$$= \phi(\zeta) T^n.$$

Since $\phi(\zeta)$ is quadratic in ζ in the denominator (recall that $w \ge 0$) and linear in ζ in the numerator, when $\Delta t \to \infty$, we have $|\zeta| \to \infty$ and so $|T^{n+1}| \to 0$. Thus the scheme is L-stable provided it is A-stable, i.e., $|\phi(\zeta)| \le 1$.

Let
$$\zeta = \nu + i\delta$$
, $\nu \ge 0$. Then $|\phi(\zeta)|^2 = \phi(\zeta)\phi(\overline{\zeta}) = \gamma/\mu$, where

$$\begin{split} \gamma &= 36[(\nu(w-1)+3)^2 + \delta^2(w-1)^2], \\ \mu &= [18+6(2+w)\zeta + (3+w)\zeta^2][18+6(2+w)\bar{\zeta} + (3+w)\bar{\zeta}^2] \\ &= 324+108(2+w)(\bar{\zeta}+\zeta) + 18(3+w)(\bar{\zeta}^2+\zeta^2) + 36(2+w)^2|\zeta|^2 + 6(2+w)(3+w)|\zeta|^2(\bar{\zeta}+\zeta) + (3+w)^2|\zeta|^4 \\ &= \nu^4(w+3)^2 + 12\nu^3(w^2+5w+6) + 2\nu^2\left[\delta^2(w+3)^2 + 18(w^2+5w+7)\right] \\ &+ 12\nu(w+2)\left[\delta^2(w+3) + 18\right] + \delta^4(w+3)^2 + 36\delta^2(w^2+3w+1) + 324. \end{split}$$

We can compute

$$\begin{split} \mu - \gamma &= v^4 (w+3)^2 + 12 v^3 (w+2) (w+3) + 2 v^2 \left(\delta^2 (w+3)^2 + 18 (7w+6) \right) \\ &+ 12 v \left[\delta^2 (w+2) (w+3) + 54 \right] + \delta^4 (w+3)^2 + 180 \delta^2 w \geq 0. \end{split}$$

So, indeed, $|\phi(\zeta)|^2 = \gamma/\mu \le 1$. Thus, in terms of von Neumann stability analysis, the scheme is unconditionally L-stable for the linear equation when u is smooth.

6. Definiton of the smoothness indicator for the adaptive Runge-Kutta method

We suggest using smoothness indicator (3.15), but there are other possibilities. Here we show results of testing various candidates for the Radau IIA smoothness indicator on the nonlinear Burgers equation (4.10). Tests applied to the Buckley-Leverett equation are not shown here because similar trends were observed. For simplicity, we suppose here that the wave speed is positive.

We begin with the simplest definitions for the Radau IIA smoothness indicator. These include detecting a shock in space using only one time level, i.e.,

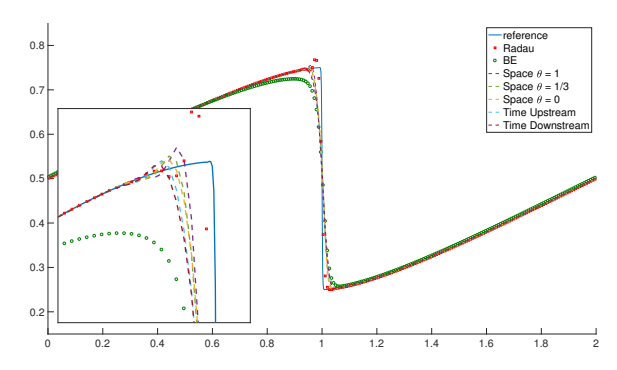
$$\sigma_{i\pm 1/2}^{\text{Radau}} = (\bar{u}_{i\pm 1}^{n+\theta} - \bar{u}_{i}^{n+\theta})^{2}, \text{ where } \theta \in \{0, 1/3, 1\},$$

and detecting a shock in time using either the upstream, i.e.,

$$\sigma^{\text{Radau}}_{i+1/2} = (\bar{u}^{n+1}_i - \bar{u}^n_i)^2 \quad \text{and} \quad \sigma^{\text{Radau}}_{i-1/2} = (\bar{u}^{n+1}_{i-1} - \bar{u}^n_{i-1})^2,$$

or downstream direction, i.e.,

$$\sigma_{i+1/2}^{\text{Radau}} = (\bar{u}_{i+1}^{n+1} - \bar{u}_{i+1}^{n})^2$$
 and $\sigma_{i-1/2}^{\text{Radau}} = (\bar{u}_i^{n+1} - \bar{u}_i^{n})^2$.



 $\begin{array}{c} \text{Radau} \\ \text{BE} \\ \text{O.7} \\ \text{O.7} \\ \text{O.8} \\ \text{O.8} \\ \text{O.9} \\ \text{O.$

Figure 6.1: Burgers equation with IC (4.11) at time t=2, m=256 and $\Delta t=5h$ using one difference in the smoothness indicators. The blue solid line is the reference solution. The red open squares are the third order Radau IIA results ($w^{\rm BE}=0$). The green circles are the backward Euler results ($w^{\rm BE}=1$). The dashed lines are the Radau IIA with backward Euler ($w^{\rm BE}=\Delta t^2$) with simple definitions of the Radau IIA smoothness indicator.

Figure 6.2: Burgers equation (4.10) with IC (4.11) at time t=2, m=256 and $\Delta t=5h$ using two differences in the smoothness indicators. The blue solid line is the reference solution. The red open squares are the third order Radau IIA results ($w^{\rm BE}=0$). The green circles are the backward Euler results ($w^{\rm BE}=1$). The dashed lines are the Radau IIA with backward Euler ($w^{\rm BE}=\Delta t^2$) with two-part Radau IIA smoothness indicators.

The results for these five (overly) simple definitions of the Radau IIA smoothness indicator on the nonlinear Burgers equation are shown in Fig. 6.1. Detecting a shock in space using $\theta=1$ gives the sharpest solution while taking $\theta=1/3$ and $\theta=0$ are nearly as good, but all three overshoot badly. On the other hand, detecting a shock in time using either the upstream or downstream direction produces slightly less overshoot, but the fronts are not as sharp as the space indicators. Using these simple definitions for the smoothness indicator, however, means that the adaptive scheme does not reduce to the backward Euler method enough, which causes overshooting of the solution. To further reduce the oscillations in the solution we must define a more complex Radau IIA smoothness indicator.

We now increase the complexity of the smoothness indicators by using two differences in the definition. We can detect a shock in space using two out of the three time levels, i.e.,

$$\sigma_{i\pm 1/2}^{\text{Radau}} = (\bar{u}_{i\pm 1}^{n+\theta_1} - \bar{u}_i^{n+\theta_1})^2 + (\bar{u}_{i\pm 1}^{n+\theta_2} - \bar{u}_i^{n+\theta_2})^2, \quad \text{where } (\theta_1, \theta_2) \in \{(0, 1), (1/3, 1), (0, 1/3)\}.$$

Moreover, a combination of detecting a shock in space and time is plausible using a single time level as well as the upstream time direction, i.e.,

$$\sigma_{i+1/2}^{\text{Radau}} = (\bar{u}_i^{n+1} - \bar{u}_i^n)^2 + (\bar{u}_{i+1}^{n+\theta} - \bar{u}_i^{n+\theta})^2 \quad \text{and} \quad \sigma_{i-1/2}^{\text{Radau}} = (\bar{u}_{i-1}^{n+1} - \bar{u}_{i-1}^n)^2 + (\bar{u}_{i-1}^{n+\theta} - \bar{u}_i^{n+\theta})^2, \quad \text{where } \theta \in \{0, 1/3, 1\}.$$

(Similar to the simple smoothness indicator defined solely by the downstream time direction, indicators which include a downstream time part produce either the least sharp solutions or produce results only comparable to those produced by indicators which include an upstream time part. Thus, definitions with downstream time parts are left out in order to reduce clutter.)

The results of using these two-part smoothness indicators are shown in Fig. 6.2. As expected, combining the two space levels $\theta_1 = 1/3$ and $\theta_2 = 1$ produces the best result. Overall the solutions of our numerical scheme using slightly more complex definitions of the Radau IIA smoothness indicators maintain a fairly sharp front, but continue to overshoot more than desired.

Hence, we once again increase the complexity of the smoothness indicators to three differences or more. For three-part definitions, first recall (3.15), which detects a shock in space. Furthermore, we can use a combination of detecting a shock in space and time by defining

$$\sigma_{i\pm 1/2}^{\text{Radau}} = (\bar{u}_i^{n+1} - \bar{u}_i^{n})^2 + (\bar{u}_{i\pm 1}^{n+1} - \bar{u}_{i\pm 1}^{n})^2 + (\bar{u}_{i\pm 1}^{n+\theta} - \bar{u}_i^{n+\theta})^2$$

where $\theta \in \{0, 1/3, 1\}$. Here we are using both the upstream and downstream time directions. For different θ , we see negligible differences in the solutions, so, without loss of generality, we take $\theta = 0$. The indicator we describe as *full space-time upstream* detects a shock in space using all three time levels and detects a shock in the upstream time direction, i.e.,

$$\begin{split} \sigma_{i+1/2}^{\text{Radau}} &= (\bar{u}_{i+1}^n - \bar{u}_i^n)^2 + (\bar{u}_{i+1}^{n+1/3} - \bar{u}_i^{n+1/3})^2 + (\bar{u}_{i+1}^{n+1} - \bar{u}_i^{n+1})^2 + (\bar{u}_i^{n+1/3} - \bar{u}_i^n)^2 + (\bar{u}_i^{n+1} - \bar{u}_i^{n+1/3})^2, \\ \sigma_{i-1/2}^{\text{Radau}} &= (\bar{u}_{i-1}^n - \bar{u}_i^n)^2 + (\bar{u}_{i-1}^{n+1/3} - \bar{u}_i^{n+1/3})^2 + (\bar{u}_{i-1}^{n+1} - \bar{u}_i^{n+1/3} - \bar{u}_{i-1}^n)^2 + (\bar{u}_{i-1}^{n+1/3} - \bar{u}_{i-1}^n)^2 + (\bar{u}_{i-1}^{n+1/3} - \bar{u}_{i-1}^{n+1/3})^2. \end{split}$$

The indicator we describe as *full space-time* is the full space-time upstream indicator, but also uses the downstream time direction, i.e.,

$$\begin{split} \sigma^{\text{Radau}}_{i\pm 1/2} &= (\bar{u}^n_{i\pm 1} - \bar{u}^n_i)^2 + (\bar{u}^{n+1/3}_{i\pm 1} - \bar{u}^{n+1/3}_i)^2 + (\bar{u}^{n+1}_{i\pm 1} - \bar{u}^{n+1}_i)^2 \\ &+ (\bar{u}^{n+1/3}_i - \bar{u}^n_i)^2 + (\bar{u}^{n+1}_i - \bar{u}^{n+1/3}_i)^2 + (\bar{u}^{n+1/3}_{i\pm 1} - \bar{u}^n_{i\pm 1})^2 + (\bar{u}^{n+1}_{i\pm 1} - \bar{u}^{n+1/3}_{i\pm 1})^2. \end{split}$$

The results of the numerical scheme using these more complex smoothness indicators of three differences or more are shown in Fig. 6.3. Although all still overshoot, it is to a slightly less degree than we have seen in previous cases. Moreover, the most involved definitions of more than three differences do not produce significant improvements in the solution compared to some of the simpler definitions. Thus, we cannot justify the decrease in computational efficiency required to use such complex indicators.

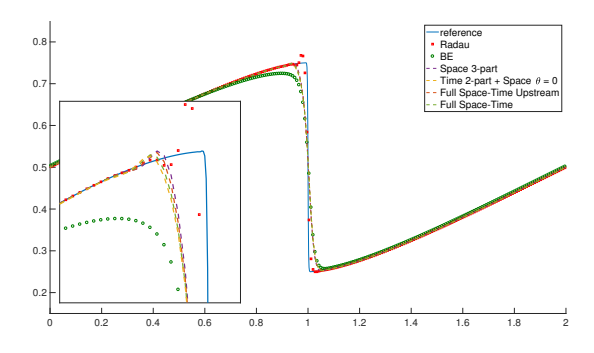


Figure 6.3: Burgers equation (4.10) with IC (4.11) at time t = 2, m = 256 and $\Delta t = 5h$ using three or more differences in the smoothness indicator. The blue solid line is the reference solution. The red open squares are the third order Radau IIA results ($w^{BE} = 0$). The green circles are the backward Euler results ($w^{BE} = 1$). The dashed lines are the Radau IIA with backward Euler ($w^{BE} = \Delta t^2$) with complex definitions of the Radau smoothness indicator.

The decision of how to define the Radau IIA smoothness indicator is a balance of finding the appropriate amount of complexity in order to reduce oscillations in the solution, yet maintain a fairly sharp front. From the analysis above the best candidates to achieve such a balance are the indicators with two or three differences. We can narrow down this large pool of candidates by increasing the CFL number. As the CFL number is increased, the solutions from

indicators with a time component quickly drop to backward Euler in these one-dimensional tests, but not the solutions which use smoothness indicators that only had space components, see Fig. 6.4. The reason for this observed behavior is that the shock touches many mesh cells in space over the time interval when the time step used represents a high CFL number. On the one hand, the indicators with a time component see the shock at each of these cells, and so backward Euler is used for all these cells. On the other hand, the three-part space indicator sees the shock only near the three times t^n , $t^{n+1/3}$, and t^{n+1} ; that is, at far fewer mesh cells. So the scheme drops to backward Euler for many fewer cells, and the solution follows the Radau IIA results better. In summary, we have narrowed down the choice of smoothness indicator to the two and three-part space indicators. Our choice of (3.15), the three-part space at all time levels, is a nice balance of competing interests, at least in one space dimension.

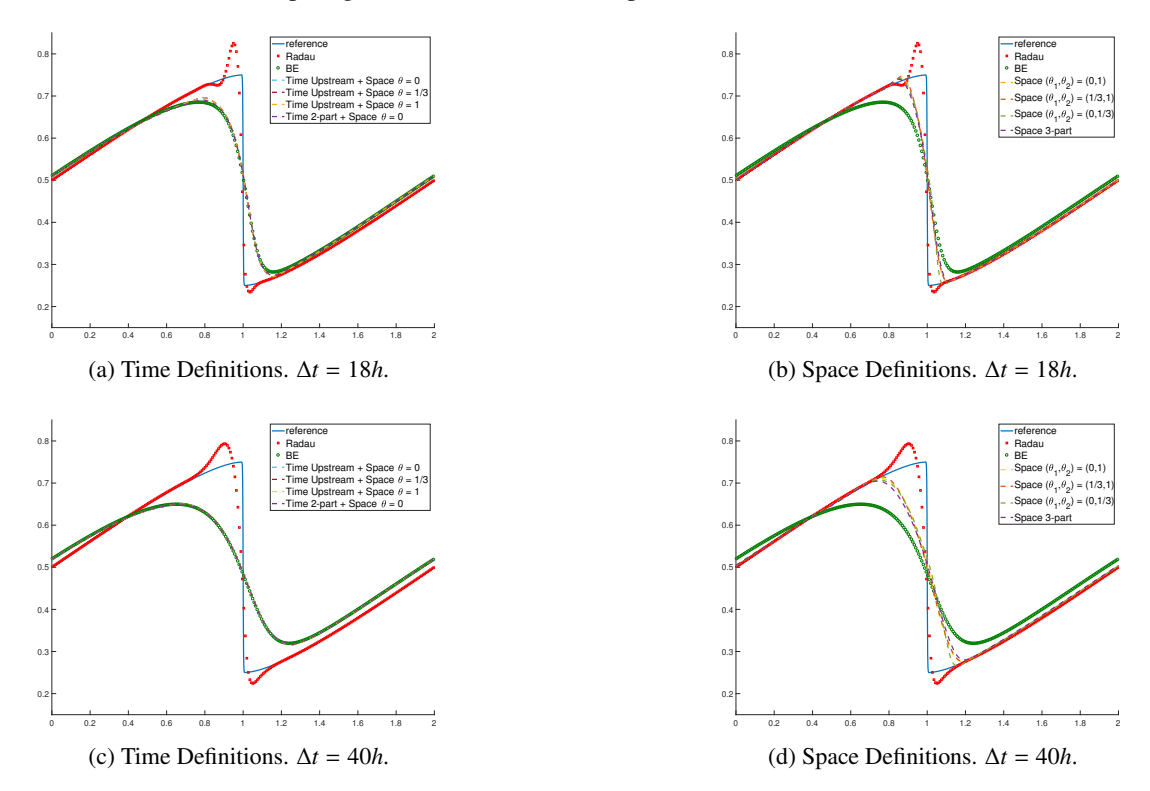


Figure 6.4: Burgers equation (4.10) with IC (4.11) at time t = 2 and m = 256 at a high CFL number. The blue solid lines are the reference solution. The red open squares are the third order Radau IIA results ($w^{BE} = 0$). The green circles are the backward Euler results ($w^{BE} = 1$). The dashed lines are the Radau IIA with backward Euler ($w^{BE} = \Delta t^2$) with smoothness indicators with or without a time component.

7. Numerical results

We present examples of our numerical scheme to test its accuracy and performance. We compare the results of third order Radau IIA, the adaptive scheme combining Radau IIA with backward Euler (using smoothness indicator (3.15)), backward Euler, and third order implicit SSP methods with two stages (s = 2). We use WENO-AO(3,2) and WENO-AO(4,3) spatial reconstructions for a third order scheme. Unless otherwise stated, all the tests in this section use a uniform grid with m elements, $\Delta x_i = h$, $\epsilon = h^2$ and $\eta = 2$.

7.1. Burgers equation

We test the schemes on the nonlinear Burgers equation with the smooth initial condition (4.11). The results shown in Fig. 7.1 use m = 256 grid cells. The SSP coefficient is c = 2.73. When $\Delta t = 3h$, all the schemes seem to work well. The Radau IIA with backward Euler is more diffusive than the Radau IIA scheme but has a higher resolution than the backward Euler scheme. When $\Delta t = 5h$, the Radau IIA with backward Euler scheme reduces oscillations near the

shock compared to the Radau IIA. For the longer timestep, the SSP scheme has excessive oscillation, and is in fact unstable.

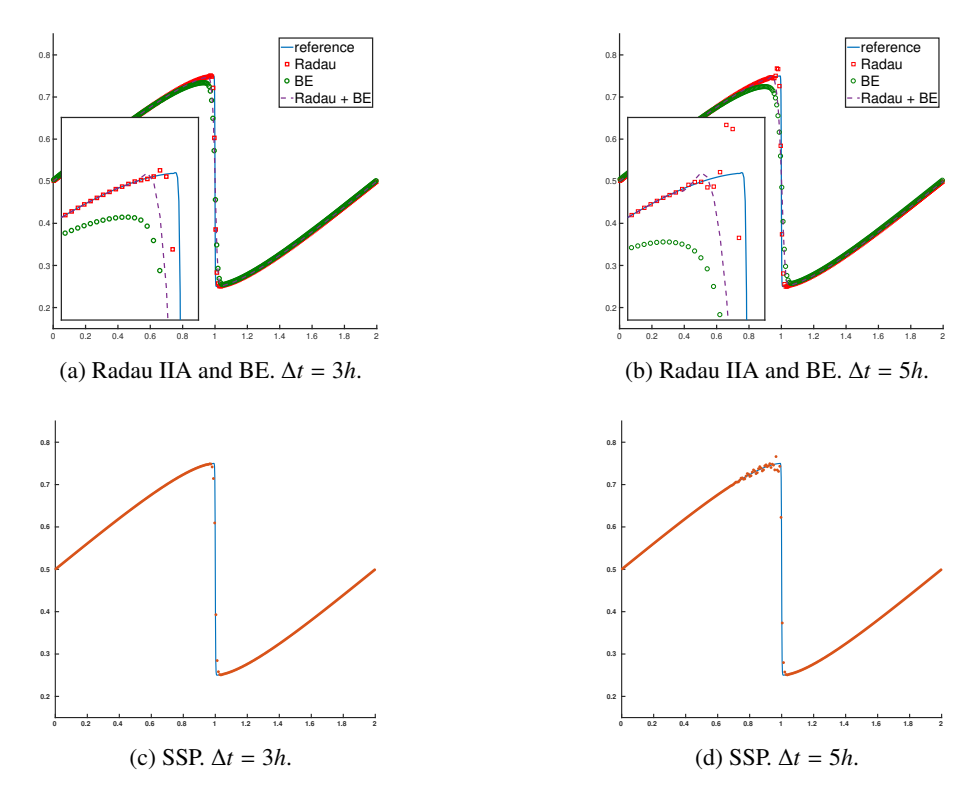


Figure 7.1: Burgers equation (4.10) with smooth IC (4.11) at time t = 2 and m = 256. The blue solid lines are the reference solution. In (a) and (b), the red open squares are the third order Radau IIA results ($w^{\text{BE}} = 0$). The purple dashed lines are the Radau IIA with backward Euler ($w^{\text{BE}} = \Delta t^2$). The green circles are the backward Euler results ($w^{\text{BE}} = 1$). In (c) and (d), the red dots are the third order implicit SSP method (s = 2).

We now take the step function (4.12) as the initial condition with a=1 and b=0. Recall that the shock travels with speed 1/2. In Figs. 7.2a and 7.2b we see that the new adaptive scheme can capture the shock and is more stable than Radau IIA when using a large timestep. In contrast, for this problem, the adaptive scheme is not better than the backward Euler scheme for both $\Delta t = 2h$ and $\Delta t = 10h$, since the true solution is piecewise constant. Fig. 7.2d shows the (unstable) third order SSP scheme produces more oscillations using $\Delta t = 5h$ than Radau IIA using $\Delta t = 10h$.

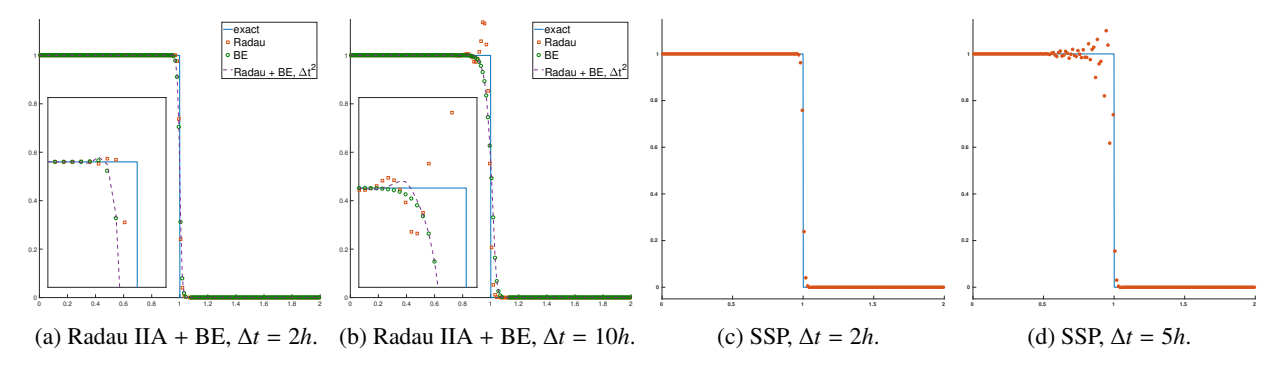


Figure 7.2: Burgers equation (4.10) with Riemann IC (4.12) at time t = 1 and m = 160. The blue solid lines are the reference solution. In (a) and (b), the red open squares are the third order Radau IIA results ($w^{BE} = 0$). The purple dashed lines are the Radau IIA with backward Euler ($w^{BE} = \Delta t^2$). The green circles are the backward Euler results ($w^{BE} = 1$). In (c) and (d), the red dots are the third order implicit SSP method (s = 2).

7.2. Buckley-Leverett equation

The next example uses the nonconvex Buckley-Leverett flux function

$$f(u) = \frac{u^2}{u^2 + \frac{1}{3}(1 - u)^2},\tag{7.1}$$

for which $\delta = \max_{u \in [0,1]} |f'(u)| = 2.2057$. We take the step function in (4.12) with a = 1 and b = 0 as the initial condition on [0, 1] with periodic boundary conditions. We use m = 100. Fig. 7.3 shows the results of the four schemes. The results are very similar when $\Delta t = 0.005$ (CFL 1.1). But when $\Delta t = 0.02$ (CFL 4.4), we see the Radau IIA with backward Euler is an improvement over the Radau IIA results, though it overshoots slightly. The SSP method also becomes unstable.

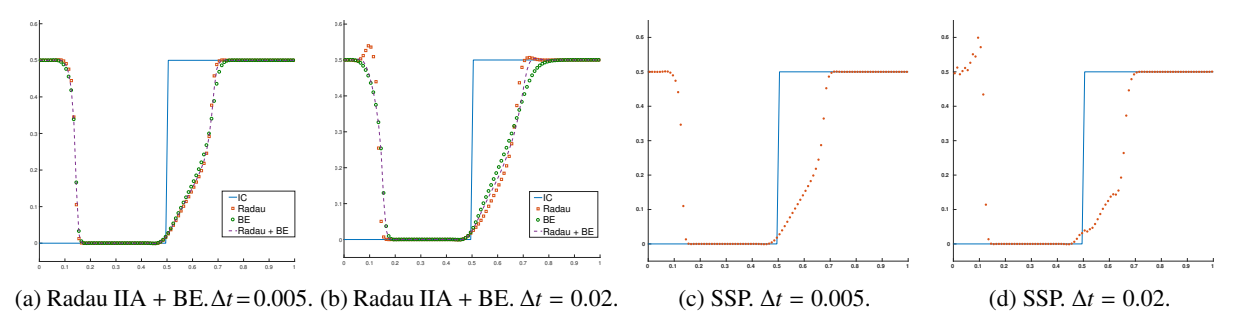


Figure 7.3: Buckley-Leverett equation at time t = 0.085 and m = 100. The blue solid lines are the initial condition. In (a) and (b), the red open squares are the third order Radau IIA results ($w^{BE} = 0$). The purple dashed lines are the Radau IIA with backward Euler ($w^{BE} = \Delta t^2$). The green circles are the backward Euler results ($w^{BE} = 1$). In (c) and (d), the red dots are the third order implicit SSP method (s = 2).

7.3. Burgers equation with diffusion

We now consider Burgers equation with linear diffusion,

$$u_t + (u^2/2)_x - Du_{xx} = 0, \quad x \in \mathbb{R}, \ t > 0,$$
 (7.2)

where D is assumed to be small, i.e., the equation is advection dominated. Exact solutions can be found using the Hopf-Cole transformation, and we take the exact solution

$$u(x,t) = \frac{-2D\pi\cos(\pi x)\exp(-D\pi^2 t)}{2 + \sin(\pi x)\exp(-D\pi^2 t)}.$$
 (7.3)

We show the results for $D=0.1,\ 0.01,\ 0.001$, with $\Delta t=10.5h$ in Table 7.1. We see the expected convergence rates, and that the errors are not appreciably worse as $D\to 0$ (in fact, they *improve* in this test).

We now take the step function (4.12) as initial condition. The exact solution is

$$u(x,t) = a + \frac{b-a}{1 + h(y,t)\exp\left(\frac{b-a}{2D}(y-ct)\right)}, \quad h(y,t) = \frac{1 - \operatorname{erf}\left(\frac{y-at}{\sqrt{4Dt}}\right)}{1 - \operatorname{erf}\left(-\frac{y-bt}{\sqrt{4Dt}}\right)},$$

where y = x - 1/2 and c = (a + b)/2. We take a = 1, b = 0.1, and D = 0.01. The results in Fig. 7.4 show that the value of w^{BE} affects the sharpness of the solution near the shock. The adaptive Radau IIA with backward Euler scheme approximates the steep front very well. When using $w^{\text{BE}} = h^2$, the results are slightly better than when using $w^{\text{BE}} = \Delta t^2$, but then the solution overshoots more when the timestep is large.

	L_h^1		L_h^{∞}				
m	error "	order	error "	order			
	1	O = 1E-0	1				
320	1.36E-04	2.56	1.19E-04	2.56			
640	1.93E-05	2.82	1.67E-05	2.82			
1280	2.50E-06	2.95	2.17E-06	2.95			
	D = 1E-02						
320	5.36E-08	2.97	6.15E-08	2.97			
640	6.72E-09	2.99	7.72E-09	2.99			
1280	8.47E-10	2.99	9.73E-10	2.99			
D = 1E-04							
320	1.86E-12	2.96	4.20E-12	2.95			
640	2.36E-13	2.98	5.33E-13	2.98			
1280	2.96E-14	2.99	6.71E-14	2.99			

Table 7.1: Smooth solution to Burgers equation with diffusion. Error and convergence order at T=1 with $\Delta t=10.5h$.

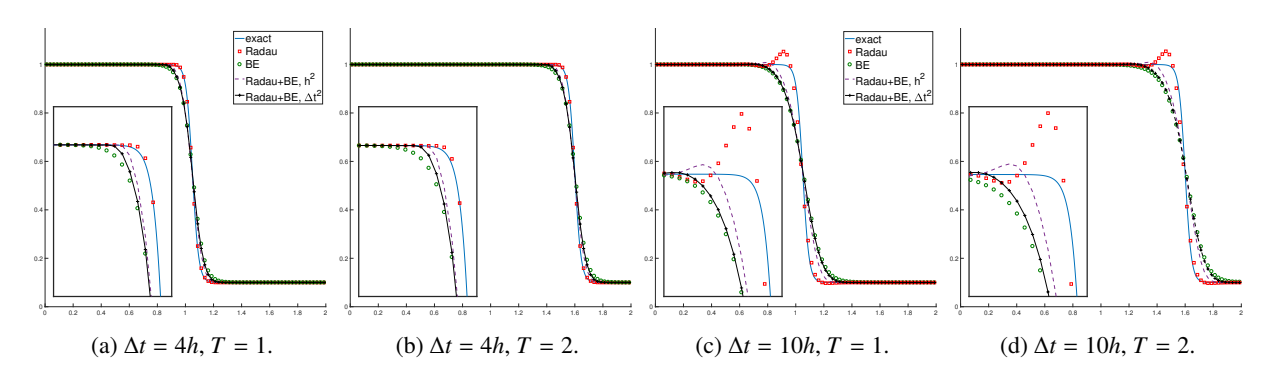


Figure 7.4: Burgers equation with diffusion and step IC (4.12). The blue solid lines are the exact solutions. The red open squares are the third order Radau IIA results ($w^{BE}=0$). The green circles are the backward Euler results ($w^{BE}=1$). The purple dashed lines are the Radau IIA with backward Euler and $w^{BE}=h^2$. The black solid line with '+' signs are the Radau IIA with backward Euler and $w^{BE}=h^2$.

7.4. Numerical results in 2D

We now give results of the adaptive Runge-Kutta method in two space dimensions using second order Strang splitting [18]. For these tests, we impose periodic boundary conditions and use an $m \times m$ uniform rectangular mesh with edge length h.

We begin with examples for the two dimensional Burgers equation

$$u_t + (u^2/2)_x + (u^2/2)_y = 0.$$

First, we impose the initial condition (IC)

$$u(x, y, 0) = 0.5 - 0.25 \sin(\pi(x + y)), \quad (x, y) \in [0, 2]^2.$$
 (7.4)

We use a 256×256 uniform grid and take $\Delta t = 5h$. Figure 7.5 shows the result of the adaptive Runge-Kutta method at t = 2. As in the one dimensional case, the scheme appears to give results with only slight oscillation near the shock. Second, we again consider the two dimensional Burgers equation but now impose the initial condition (IC)

$$u(x, y, 0) = \sin^2(\pi x)\sin^2(\pi y), \quad (x, y) \in [0, 2]^2.$$
(7.5)

For this example we use a 160×160 uniform grid and take $\Delta t = 4h$. Figure 7.6 shows the result of the adaptive method at t = 0, 0.75, and 1.5. The scheme resolves the shock well.

Finally, we consider the rotation of a square patch on $[0, 1]^2$ using the equation

$$u_t - ((y - 1/2)u)_x + ((x - 1/2)u)_y = 0. (7.6)$$

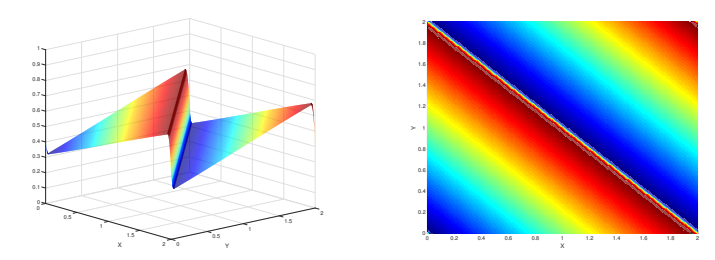


Figure 7.5: Burgers equation with IC (7.4) using m = 256 and $\Delta t = 5h$ at t = 2.

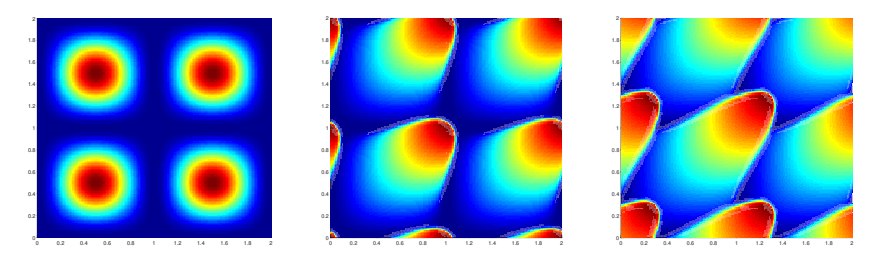


Figure 7.6: Burgers equation with IC (7.5) using m = 160 and $\Delta t = 4h$ at t = 0, 0.75, and 1.5.

We use a 160×160 uniform grid and take $\Delta t = 3\pi h$. Figure 7.7 shows the results after rotations of $\pi/4$ and $\pi/2$. For a large timestep, such as $\Delta t = 4\pi h$, Newton's method does not converge if the smoothness indicator used in the adaptive Runge-Kutta scheme lacks a time component. The scheme reverts to composite backward Euler time-stepping over a larger region of space than when there are no time components in the smoothness indicator, and so the overall scheme is more numerically diffusive. This makes the problem easier to solve, and Newton's method converges. But, of course, the solution is no better than what composite backward Euler gives, so we prefer to limit the time step and use the smoothness indicator (3.15) based on detecting a shock only in space.

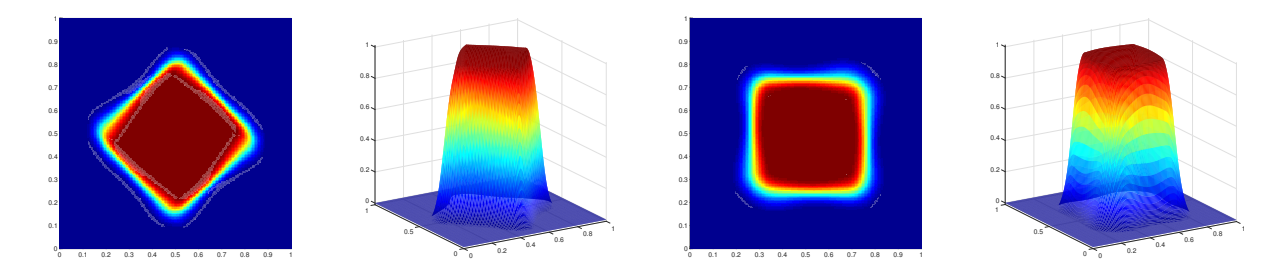


Figure 7.7: Rigid body rotation using m = 160 and $\Delta t = 3\pi h$ at $t = \pi/4$ (left two figures) and $t = \pi/2$ (right two figures).

8. Summary and Conclusions

We developed a finite volume approximation of the scalar hyperbolic conservation law or advection-diffusion equation suitable for using timesteps longer than the CFL timestep. The space discretization uses weighted essentially non oscillatory reconstructions with adaptive order (WENO-AO). The time evolution uses an adaptive Runge-Kutta method which is a weighted combination of a high order implicit Runge-Kutta method and the composite backward Euler method.

Because SSP methods are only conditionally stable, and the stability constraint is close to the CFL limited timestep, we needed to use other Runge-Kutta methods. Because the advection-diffusion equation is stiff, the L-stable, implicit, third order Radau IIA method was chosen, even though it can produce some oscillation in the solution near discontinuities or steep fronts. To reduce these oscillations, the method reverts to composite backward Euler

near discontinuities, using a weighting procedure inspired from standard spatial WENO methods. We proved that the weighted scheme was third order accurate for smooth solutions, and we saw computationally that the scheme maintains third order accuracy away from discontinuities, and overall reduces to the accuracy of the backward Euler scheme. We also saw that the adaptive Runge-Kutta method was successful in reducing oscillations in the solution. We also proved, via a von Neumann stability analysis, that the scheme is unconditionally L-stable for the linear problem, at least when the solution is smooth.

We considered many possible definitions of the smoothness indicator needed to weight the adaptive Runge-Kutta method. We concluded that simple indicators do not reduce the oscillations enough, and that indicators that include a difference in time reduce to backward Euler when using very long timesteps (i.e., at high CFL number). We therefore advocated for the use of (3.15), which measures smoothness only in space, but at all three time levels.

We conclude that our new scheme is successful in handling the 1D scalar hyperbolic conservation law (and advection-diffusion equation) using relatively long timesteps. Future work might consider whether some theory could be developed to adjust the scheme's parameters (such as w_0^{BE} , ϵ_0 , and η) to minimize the oscillations in the solution. Moreover, future work might consider the definition of the adaptive Runge-Kutta smoothness indicators when using methods higher than third order, and also when solving systems of equations. We successfully solved 2D problems using second order Strang time splitting. Future work might also consider genuine 2D schemes for nonrectangular computational meshes (the use of WENO-AO allows the spatial reconstructions to work well in this case [21, 17]).

Acknowledgements

The work of Arbogast and Zhao was supported in part by the U.S. National Science Foundation under grant DMS-1418752. The work of Arbogast and King was supported in part by the U.S. National Science Foundation under grant DMS-1912735. The work of Huang was supported in part by Taiwan Ministry of Science and Technology grant MOST 107-2115-M-110-004-MY2, National Center for Theoretical Sciences, Taiwan, and the Multidisciplinary and Data Science Research Center of the National Sun Yat-sen University.

References

- [1] D. S. Balsara, S. Garain, C.-W. Shu, An efficient class of WENO schemes with adaptive order, J. Comput. Phys. 326 (2016) 780-804.
- [2] I. Cravero, G. Puppo, M. Semplice, G. Visconti, CWENO: Uniformly accurate reconstructions for balance laws, Math. Comp. 87 (2018) 1689–1719. doi:10.1090/mcom/3273.
- [3] T. Arbogast, C.-S. Huang, X. Zhao, Accuracy of WENO and adaptive order WENO reconstructions for solving conservation laws, SIAM J. Numer. Anal. 56 (3) (2018) 1818–1847, DOI 10.1137/17M1154758.
- [4] C.-W. Shu, Total-variation-diminishing time discretizations, SIAM J. Sci. Statist. Comput. 9 (1988) 1073-1084.
- [5] S. Gottlieb, C.-W. Shu, Total variation diminishing Runge-Kutta schemes, Math. Comp. 67 (1998) 73-85.
- [6] D. I. Ketcheson, C. B. Macdonald, S. Gottlieb, Optimal implicit strong stability preserving Runge-Kutta methods, Applied Numerical Mathematics 59 (2009) 373–392.
- [7] S. Gottlieb, C.-W. Shu, E. Tadmor, Strong stability preserving high-order time discretization methods, SIAM Review 43 (2001) 73–85.
- [8] S. Osher, R. Sanders, Numerical approximations to nonlinear conservation laws with locally varying time and space grids, Mathematics of Computation 41 (164) (1983) 321–336.
- [9] H.-Z. Tang, G. Warnecke, High resolution schemes for conservation laws and convection-diffusion equations with varying time and space grids, Journal of Computational Mathematics (2006) 121–140.
- [10] E. M. Constantinescu, A. Sandu, Multirate timestepping methods for hyperbolic conservation laws, Journal of Scientific Computing 33 (3) (2007) 239–278.
- [11] D. I. Ketcheson, C. B. MacDonald, S. J. Ruuth, Spatially partitioned embedded Runge-Kutta methods, SIAM Journal on Numerical Analysis 51 (5) (2013) 2887–2910.
- [12] W. Hundsdorfer, D. I. Ketcheson, I. Savostianov, Error analysis of explicit partitioned Runge–Kutta schemes for conservation laws, Journal of Scientific Computing 63 (3) (2015) 633–653.
- [13] M. Günther, A. Kvaernø, P. Rentrop, Multirate partitioned runge-kutta methods, BIT Numerical Mathematics 41 (3) (2001) 504-514.
- [14] W. Hundsdorfer, A. Mozartova, V. Savcenco, Monotonicity conditions for multirate and partitioned explicit Runge-Kutta schemes, in: Recent developments in the numerics of nonlinear hyperbolic conservation laws, Springer, 2013, pp. 177–195.
- [15] D. Kuzmin, M. Q. de Luna, C. E. Kees, A partition of unity approach to adaptivity and limiting in continuous finite element methods, Computers & Mathematics with Applications 78 (3) (2019) 944–957.
- [16] B. Cockburn, C. Johnson, C.-W. Shu, E. Tadmor, Advanced Numerical Approximation of Nonlinear Hyperbolic Equations, Vol. 1697 of C.I.M.E. Foundation Subseries, Springer, Berlin, Heidelberg, 1998, lectures given at the 2nd Session of the Centro Internazionale Matematico Estivo (C.I.M.E.) held in Cetraro, Italy, June 23-28, 1997.
- [17] T. Arbogast, C.-S. Huang, X. Zhao, Finite volume WENO schemes for nonlinear parabolic problems with degenerate diffusion on non-uniform meshes, J. Comput. Phys. 399, DOI 10.1016/j.jcp.2019.108921.

- [18] G. Strang, On the construction and comparison of difference schemes, SIAM. J. Numer. Anal. 5 (3) (1968) 506-517.
- [19] G.-S. Jiang, C.-W. Shu, Efficient implementation of weighted ENO schemes, J. Comput. Phys. 126 (1996) 202-228.
- [20] D. Levy, G. Puppo, G. Russo, Compact central WENO schemes for multidimensional conservation laws, SIAM J. Sci. Comput. 22 (2) (2000) 656–672.
- [21] T. Arbogast, C.-S. Huang, X. Zhao, Von Neumann stable, implicit, high order, finite volume WENO schemes, in: SPE Reservoir Simulation Conference 2019, Society of Petroleum Engineers, Galveston, Texas, 2019, pp. 1–16, sPE-193817-MS.
- [22] E. Hairer, G. Wanner, Solving ordinary differential equations II: Stiff and differential-algebraic problems, 2nd Edition, Springer-Verlag, Berlin, New York, 1996.
- [23] F. Aràndiga, A. Baeza, A. M. Belda, P. Mulet, Analysis of WENO schemes for full and global accuracy, SIAM J. Numer. Anal. 49 (2) (2011) 893–915.
- [24] N. N. Kuznetsov, On stable methods for solving non-linear first order partial differential equations in the class of discontinuous functions, in: Topics in numerical analysis III, Royal Irish Academy, Academic Press, London, 1977, pp. 183–197.
- [25] R. J. LeVeque, Numerical Methods for Conservation Laws, 2nd Edition, Birkhäuser, Basel, 1992.
- [26] J. C. Strikwerda, Finite Difference Schemes and Partial Differential Equations, 2nd Edition, SIAM, Philadelphia, 2004.